Digital Comprehensive Summaries of Uppsala Dissertations
from the Faculty of Science and Technology 2451

Towards an Integrated Optoelectronic Device for Single-Molecule Detection in Electrolytes

YUPENG YANG

ACTA UNIVERSITATIS
UPSALIENSIS
2024

ISSN 1651-6214
ISBN 978-91-513-2234-6
urn:nbn:se:uu:diva-538768

UPPSALA
UNIVERSITET

Dissertation presented at Uppsala University to be publicly examined in 10132, Häggsalen, Ångström, Regementsvägen 1, Ångströmlab, Uppsala, Thursday, 7 November 2024 at 13:15 for the degree of Doctor of Philosophy. The examination will be conducted in English. Faculty examiner: Professor Carsten Ronning (Friedrich Schiller University Jena).

Abstract
Yang, Y. 2024. Towards an Integrated Optoelectronic Device for Single-Molecule Detection in Electrolytes. *Digital Comprehensive Summaries of Uppsala Dissertations from the Faculty of Science and Technology* 2451. 75 pp. Uppsala, Sweden: Acta Universitatis Upsaliensis. ISBN 978-91-513-2234-6.

Single-molecule detection (SMD) provides ultrahigh sensitivity in biosensing and bioimaging, which is crucial for DNA and protein sequencing, early disease diagnose, drug detection, environment monitoring, food safety, and a deeper understanding of biological process, etc. Among various methods developed for SMD, fluorescence-based methods and transistor-based methods are outstanding due to their high sensitivity and versatility. However, fluorescence-based methods usually rely on labels, and advanced but bulky and expensive microscopes, restricting them to research use. For the label-free nanoscale field-effect transistors (FETs), detections of charged molecules of nanometres or larger in size are dubious due to the so-called Debye screening effect.

Here in this thesis, a novel optoelectronic device for molecular sensing is developed, combining the advantages of fluorescence-based methods and FET-based methods, while avoiding their disadvantages. Hydrogendoped amorphous InGaZnO thin film-based transistors (a-IGZO:H TFTs) are employed as phototransistors to detect photoluminescence signals from the upconversion nanoparticles (UCNPs) immobilized on top of the a-IGZO:H active layer. Molecular sensing is demonstrated using UCNP-based Förster resonance energy transfer (FRET) with streptavidin-biotin bonding pairs and small gold nanoparticles as quenchers. The integration of UCNPs and FRET with phototransistors simplifies the optics and gives a high signal-noise ratio (SNR). The integrated setup is promising to be developed into a portable and cost-effective biosensing platform with high sensitivity. To improve SNR, plasmonic nanostructures including aluminum nanohole arrays and gold nanorod dimers are simulated and fabricated to enhance the fluorescence intensities of fluorophores including single quantum dots, organic dyes on single extracellular vesicles, and single UCNPs. The plasmonic nanostructures for enhancing fluorescence intensities of single UCNPs can be integrated onto highly sensitive photodetectors in future studies to achieve SMD in electrolytes.

Keywords: phototransistors, fluorescence, molecular sensing, surface plasmonics

Yupeng Yang, Department of Electrical Engineering, Solid-State Electronics, Box 65, Uppsala University, SE-751 03 Uppsala, Sweden.

ISSN 1651-6214
ISBN 978-91-513-2234-6
URN urn:nbn:se:uu:diva-538768 (http://urn.kb.se/resolve?urn=urn:nbn:se:uu:diva-538768)

To my family

List of Papers

This thesis is based on the following papers, which are referred to in the text by their Roman numerals.

I. **Yang, Y.**, Dev, A., Sychugov, I., Hägglund, C., Zhang, S. L. (2023) Plasmon-Enhanced Fluorescence of Single Quantum Dots Immobilized in Optically Coupled Aluminum Nanoholes. *The Journal of Physical Chemistry Letters*, 14, 9, 2339–2346.

II. **Yang, Y.**, Metem, P., Khaksaran M. H., Sahu S. S., Stridfeldt F., Görgens A., Zhang, S. L., Dev, A. Plasmon-Enhanced Fluorescence of Single Extracellular Vesicles Captured in Arrayed Aluminum Nanohole. (*Revised version under review with ACS Omega (August 2024)*)

III. **Yang, Y.**, Khaksaran, M.H., An, J. B., Lee, S., Kim, H. J., Johansson, T., Lu, X., Sychugov, I., Dev, A., Zhang, S. L. Phototransistors of Engineered InGaZnO Channel for Specific Molecular Detection in the Visible Range. *(Revised version under review with ACS Applied Optical Materials (September 2024))*

IV. **Yang, Y.,** Lu, X., Sychugov, I., Dev, A., Zhang, S. L. Plasmon-Enhanced Photoluminescence of Single Upconversion Nanoparticles Site-Selectively Captured between Gold Nanorods (*Manuscript*)

Author's contributions

I. Conceived the idea, planned and conducted the major part of the work including simulation, fabrication, fluorescence imaging, and data analysis. Wrote and revised the manuscript according to referee comments.

II. Planned and performed simulation, device pattern design, and fluorescence imaging. Took part in discussion and data analysis. Wrote and revised the manuscript according to referee comments.

III. Planned and conducted the major part of the work including device pattern design, device fabrication, electrical measurements, integration of measurement setup, fluorescence imaging, and optoelectronic measurements. Took part in discussion and data analysis. Wrote and revised the manuscript according to referee comments.

IV. Conceived the idea, planned and conducted all the experimental work including simulation, fabrication, and photoluminescence imaging. Took part in discussion and data analysis. Wrote the manuscript.

Publications not included in this thesis

I. Pham, N.*, Khaksaran, M. H., *, Lee, W. Y.*, **Yang, Y. P.**, Wen, C. Y., Zhang, S. L. Plasmonic Slit Nanopore Arrays to Enhance Nanoparticle Loading and Amplify Fluorophore Signals. (Manuscript).

*The authors contributed equally to the work.

Contents

Abbreviations

AFM	Atomic force microscopy
Al	Aluminum
ALD	Atomic layer deposition
Al_2O_3	Aluminum oxide
AOS	Amorphous oxide semiconductor
APDs	Avalanche photodiodes
A_{spot}	Area of the laser spot
$A_{W\times L}$	Channel area between source and drain
α	Amorphous
BP	Bandpass
BSA	Bovine serum albumin
C/m^2	Coulomb per square meter
CCD	Charged-coupled device
CdSe	Cadmium selenide
CMOS	Complementary metal-oxide-semiconductor
CNDs	Carbon nanodomains
Cr	Chromium
Cy3	Cyanine3 dye
Cy5	Cyanine5 dye
D*	Detectivity of the phototransistors
DF	Darkfield
DI	Deionized
E	Electric field
E_0	Incident electric field
EBL	Electron beam lithography
EBID	Electron beam-induced deposition
EHPs	Electron-hole pairs
Er	Erbium
ET	Energy transfer
EVs	Extracellular vesicles
F	Fluorine
FEM	Finite elements method
FET	Field effect transistor
FL	Fluorescence
FRET	Förster resonance energy transfer

GNRDs	Gold nanorod dimers
HMDS	Hexamethyldisilane
HSQ	Hydrogen silsesquioxane
ICP	Inductively coupled plasma
IGZO	Indium gallium zinc oxide
IGZO: H	Hydrogenated indium gallium zinc oxide
IPA	Isopropyl alcohol
ITO	Indium tin oxide
LSPR	Localized surface plasmon resonance
MIBK	Methyl isobutyl ketone
mNG	mNeonGreen
MP	Multiphoton
mTorr	Millitorr
μPL	Micro-photoluminescence
NIR	Near infrared
NPs	Nanoparticles
NTA	Nanoparticle tracking analysis
PBS	Phosphate-buffered saline
PCB	Printed circuit board
PDMS	Polydimethylsiloxane
PEG	Poly (ethylene glycol)
PL	Photoluminescence
PLL	Poly(L-lysine)
PML	Perfectly matched layer
PMT	Photomultiplier tube
PR	Photoresponsivity of the phototransistors
PS	Photosensitivity of the phototransistors
PVPA	Poly (vinyl phosphonic acid)
QDs	Quantum dots
RCA	Radio Corporation of America
RIE	Reactive ion etching
SA	Streptavidin
SAM	Self-assembled monolayer
Sccm	Standard cubic centimeter per minute
SEM	Scanning electron microscopy
SMD	Single-molecule detection
smFRET	Single-molecule Förster resonance energy transfer
SMU	Source measure units
SNR	Signal-noise ratio
SPR	Surface plasmon resonance
SPPs	Surface plasmon polaritons
SS	Subthreshold swing
TEM	Transmission electron microscopy
TFTs	Thin film transistors

Tm	Thulium
UCNPs	Upconversion nanoparticles
UV	Ultraviolet
V_{DS}	Source-drain voltage
Vis	Visible
V_G	Gate voltage
W	Watt
WF	Widefield
Y	Yttrium
Yb	Ytterbium

1 Introduction

1.1 Single-molecule detection

The field of single-molecule studies began in the 1950s, driven by advances in experimental techniques and tools [1]. Single-molecule detection (SMD) offers ultrahigh sensitivity, making it a crucial tool in biosensing for applications such as DNA and protein sequencing, early disease diagnosis, point-of-care detection, and food safety [2]，[3]. Unlike ensemble measurements, SMD can reveal biophysical and biochemical information that is often averaged out, providing insights into the physical and chemical properties, behaviors, interactions, and dynamics of individual molecules [4], [5]. This, in turn, deepens our understanding of biological processes such as DNA transcription, protein folding, cell signaling, and molecular transport [4].

Among the various methods developed for SMD, fluorescence-based and transistor-based techniques stand out due to their high sensitivity and versatility [6]. This section provides a brief introduction to these methods.

1.1.1 Fluorescence-based methods

In 1990, the fluorescence signal from a single pentacene molecule was detected for the first time [7]. Since then, fluorescence has become a powerful and widely used method for SMD due to its high sensitivity and the availability of a broad range of fluorophores [6]. A Jablonski diagram of fluorescence is shown in Figure 1.1a, where singlet ground, first, and second electronic states of a fluorophore are depicted as S0, S1, and S2, respectively, with vibrational energy levels [8]. Transitions between states are depicted as vertical lines to illustrate absorption, internal conversion, fluorescence, intersystem crossing to the first triplet state (T1) and phosphorescence [8]. The presence and behavior of a single molecule can be inferred by detecting the emitted photons from fluorophores attached to it.

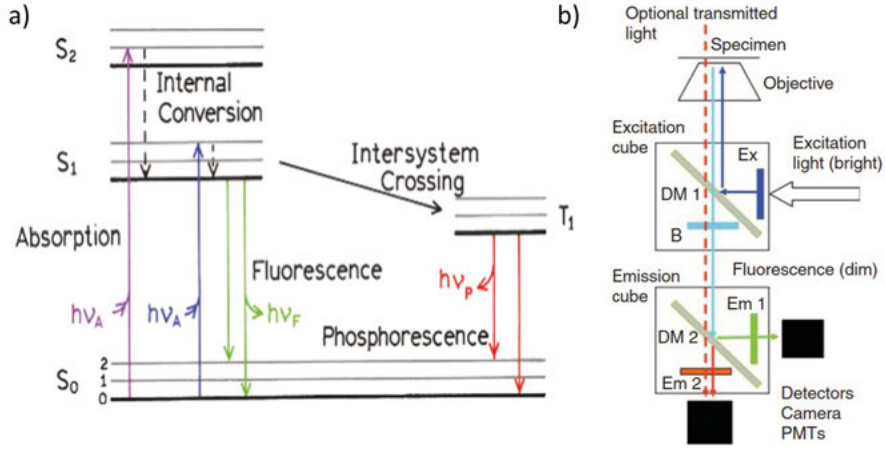

Figure 1.1 (a) A typical Jablonski diagram, reproduced from [8] with permissions. Copyright @ 2006 Springer-Verlag U. S. (b) Schematics of a fluorescence microscope, reproduced from [9] with permissions.

Both fluorescence microscopy and spectroscopy have been developed to achieve SMD [10]. Schematics of a typical fluorescence microscope is shown in Figure 1.1b, where light sources, excitation and emission filters, dichroic mirrors, objectives, and photodetectors are basic components. To detect single molecules using fluorescence-based methods, the SNR must exceed unity [10]. A quantitative expression of the SNR for fluorescence detection of a single molecule is given by:

$$SNR = \frac{D\emptyset_{\mathrm{F}}\left(\frac{\sigma_{\mathrm{P}}}{A}\right)\left(\frac{P_0}{hv}\right)T}{\sqrt{\left(\frac{D\emptyset_{\mathrm{F}}\sigma_{\mathrm{P}}P_0T}{Ahv}\right) + C_{\mathrm{b}}P_0T + N_{\mathrm{d}}T}} \tag{1}$$

Here it is assumed that the noise factors limiting detection are the Poisson (shot) noise fluctuations of the single-molecule signal, the background signal, and the dark counts [11]. In equation (1),

$$D = \eta_{\mathrm{Q}}F_{\mathrm{coll}}F_{\mathrm{opt}}F_{\mathrm{filter}} \tag{2}$$

- D is an instrument-dependent collection factor, which is the product of the detector quantum efficiency (η_{Q}) , the angular collection factor (F_{coll}), the transmission factor (F_{opt}), and the filter transmission factor (F_{filter}).
- $\emptyset_{\mathrm{F}}$ is the fluorescence quantum yield of the fluorophore.
- σ_{P} is the absorption cross-section.
- A is the beam area.
- $\frac{P_0}{hv}$ is the number of incident photons per second.

- T is the detector counting interval.
- C_{b} is the background count rate per watt of excitation power.
- N_{d} is the dark count rate.

According to Equation (1), achieving a high SNR requires the use of bright and photostable fluorophores, a small excitation volume, efficient light collection and transmission optics, and highly sensitive photodetectors, such as PMTs, APDs, and CCDs with low dark noise.

Several types of fluorescence microscopy are commonly used for imaging single molecules, including widefield epi-fluorescence microscopy, confocal microscopy, total internal reflection fluorescence (TIRF) microscopy, near-field scanning optical microscope (NSOM), multiphoton microscopy, and super-resolution microscopy [12] (Figure 1.2). Widefield epi-fluorescence microscopy with a CCD suffers from reduced SNR due to the large excitation and detection volumes but allows for the parallel detection of multiple molecules [13]. Confocal microscopy uses point detectors such as PMTs or APDs, along with pinhole apertures, to eliminate out-of-focus light, thereby reducing the excitation and detection volumes and enhancing depth resolution [10]. However, it cannot observe multiple molecules simultaneously, and scanning is typically required to obtain two-or three-dimensional fluorescence images [13]. TIRF microscopy and NSOM employ an evanescent field, which decays exponentially from the surface of a substrate or a sub-wavelength aperture, to significantly reduce the excitation volume, allowing the selective excitation of molecules within a few hundred nanometers of a surface or tiny aperture [12]. The excitation volume in multiphoton microscopy is also spatially confined due to the high-power density required by the multiphoton excitation mechanism [10]. Super-resolution techniques such as stimulated emission depletion (STED) minimize the excitation area to achieve sub-diffraction limit resolution [12].

Single molecules can be either immobilized on a substrate or freely diffusing in solution for SMD [13]. Freely diffusing single molecules can be detected using fluorescence correlation spectroscopy, which captures photon bursts as molecules enter the excitation volume within the solution [13]. In contrast, immobilized single molecules can be studied until photobleaching [13].

Single molecules can also be excited through nonradiative resonance energy transfer from another molecule usually within a 10 nm distance [14]. The efficiency of this energy transfer is highly sensitive to the intermolecular distance, a technique known as smFRET, which has been widely utilized for studying the conformational dynamics of biomolecules and for specific biosensing applications [15], [16].

Despite the advantages of fluorescence-based methods, bulky, complex, and expensive setups are always needed, which limits their accessibility and scalability and restricts them primarily to research applications.

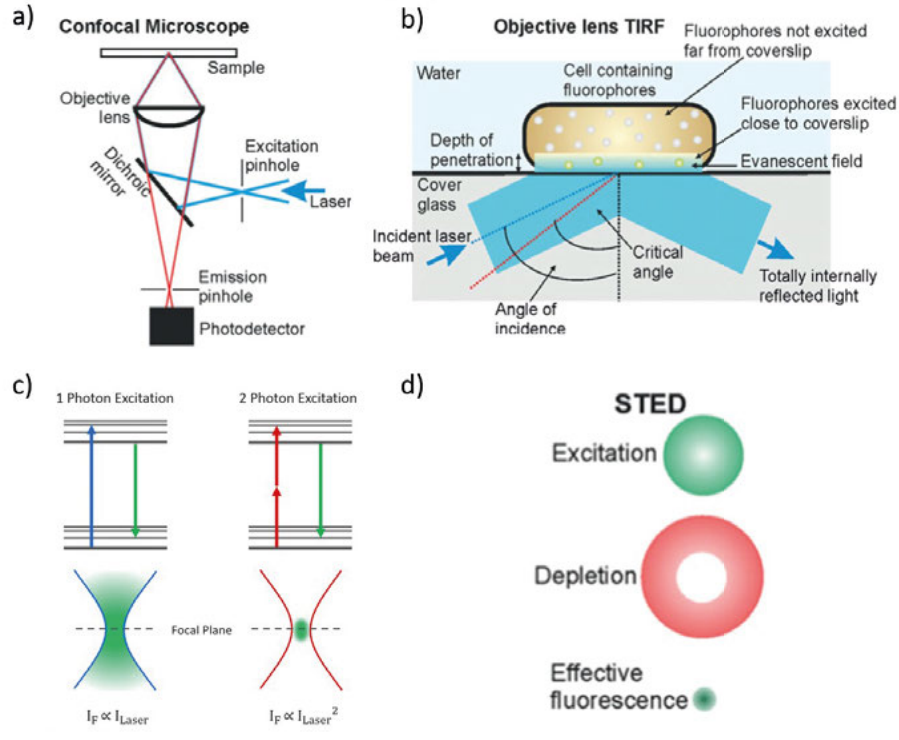

Figure 1.2 Schematics of confocal microscopy (a) and TIRF microscopy (b). Illustrated mechanisms of two-photon excitation (c) and STED technique (d). (a), (b), and (d) are reproduced from [12] with permissions. Copyrights @ 2017 The Author(s). (c) is reproduced from [17]. Copyrights @ 2022 Edinburgh Instruments.

1.1.2 Transistor-based methods

A transistor is a semiconductor device used for amplifying or switching electrical signals and power, serving as a fundamental building block of modern electronics [18]. Nanowire FETs (NWFETs) based on Si or carbon nanotubes provide label-free detection with high sensitivity and the compatibility with existing electronic devices and systems, offering a complementary approach to fluorescence-based methods [19], [20]. When a charged molecule, such as a single strand DNA or a protein or a single virus, binds to the functionalized surface of the NWFET, a variation of charge or electric potential is induced at the NW surface, which is similar to applying a gate bias in a conventional FET [21], [22]. The current change is thereby associated with molecular binding events in real time [21]–[23], see the schematics in Figure 1.3. The ultrahigh

sensitivity is due to the high surface-to-volume ratios of NWs and their small diameters similar to biomolecules [23]. However, the Debye screening effect in electrolyte makes the detection of large and charged molecules dubious [24].

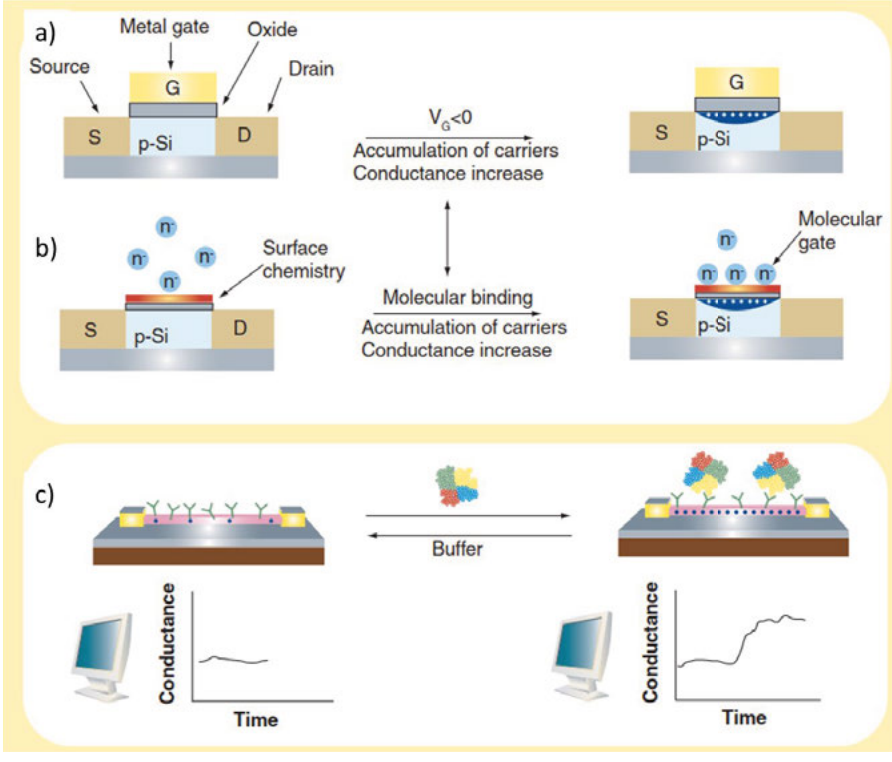

Figure 1.3 (a) Schematic of a FET device before and after applying a gate bias. (b) Schematics of a FET device used for sensing molecular binding with charges. (c) Schematics of a NWFET device with a functionalized NW surface. Binding of a protein causes an increase in the conductance. Reproduced from [22] with permissions. Copyrights @ 2006 Future Medicine Ltd.

Given these considerations, it is logical to explore the potential of integrating FETs with fluorescence detection to develop a portable and cost-effective platform for SMD. One promising approach involves the use of field effect phototransistors, which merge FETs with photosensitive materials and convert light signals into electrical outputs. When the phototransistor is exposed to light, photons with energy greater than the bandgap of the material generate electron-hole pairs (EHPs) in the photosensitive layer. The EHPs can modulate the charge in the channel, alternating the current flow between the source and drain, *i.e.* the photocurrent, which depends on the light intensity. Nanoscale phototransistors, fabricated using standard silicon technology on a chip, can function as photodetectors, capable of detecting fluorescence signals from single molecules by monitoring changes in output current associated

with single-molecule events. This approach is analogous to the photodetectors used in fluorescence microscopes. However, several critical questions below must be addressed, which are systematically explored in this thesis.

1. How can semiconductor-based phototransistors detect Stokes-shifted fluorescence signals without the need for complex optical components, such as filters?
2. How can biosensing be directly implemented on phototransistors?
3. How can the SNR of phototransistors be enhanced to achieve effective SMD?

1.2 Thesis organization

The structure of this thesis, following the introduction chapter, can be summarized as follows: Chapter 2 briefly introduces the main components investigated in this thesis, including α-IGZO thin film-based phototransistors, UCNPs, FRET, and plasmon-enhanced fluorescence. Chapter 3 demonstrates a novel integration of α-IGZO thin film-based phototransistors, UCNPs, and FRET, as a promising sensitive and specific molecular sensing platform (Paper III). Chapter 4 presents the comprehensive investigations of plasmon-enhanced fluorescence of single fluorophores using different metallic nanostructures, including Al nanohole arrays and gold nanorod dimers (GNRDs). The fluorescence intensities of single QDs (Paper I) and R-PE dyes on single EVs (Paper II) in Al nanohole arrays, and single UCNPs in the gap of GNRDs (Paper IV) are demonstrated to be enhanced by the locally-enhanced electromagnetic field.

Finally, Chapter 5 summarizes the achievements of the phototransistor-based novel molecular sensing platform and plasmon-enhanced fluorescence of single fluorophores. Outlooks towards a novel SMD platform is presented.

2 Components

2.1 α-IGZO thin film-based phototransistors

Thin-film transistors (TFTs) based on amorphous oxide semiconductors (AOS) have been extensively investigated and widely applied in large-area electronics including displays, flexible electronics, transparent electronics, integrated circuits, memory, neuromorphic systems, sensors, etc., ever since the first invention of amorphous InGaZnO (α-IGZO) TFTs in 2004 [25], see Figure 2.1. The key advantages of AOS TFTs include uniform large-area mass production, low processing temperature, low off-current, and high electron mobility (>10 $cm^2V^{-1}s^{-1}$), which is exceptional as an amorphous semiconductor, compared with conventional hydrogenated amorphous silicon TFTs [26].

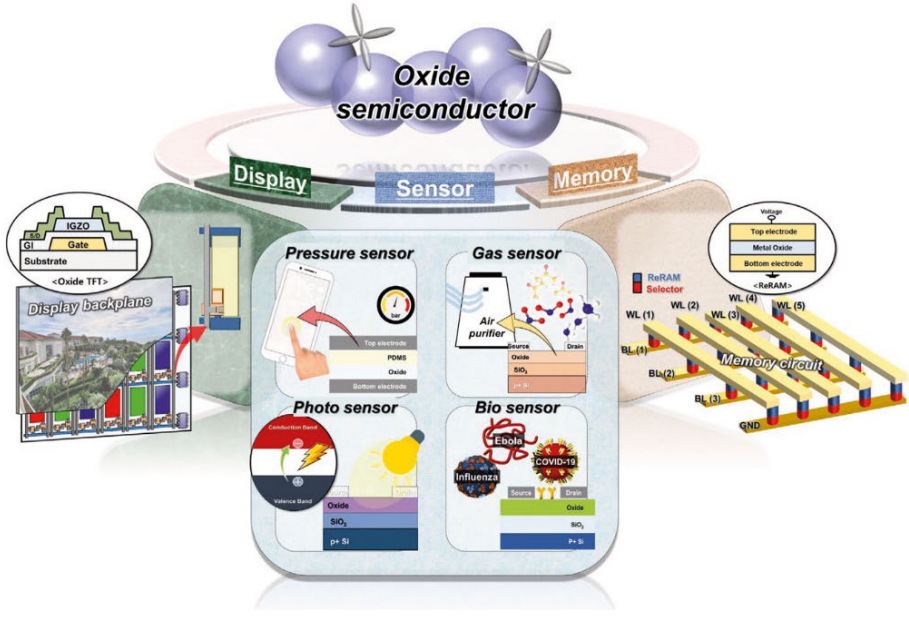

Figure 2.1 Schematic orbital drawings for the carrier transport paths in oxide semiconductors and their applications in display, sensor, and memory. Reproduced from [27] with permissions. Copyright © 2021 Wiley-VCH GmbH.

Since α-IGZO is a direct energy gap (bandgap) semiconductor, it has a high quantum efficiency in absorbing incident photons and generating EHPs.

Research interest in applying α-IGZO TFTs as phototransistors has sharply increased during the past decade [27]. However, the wide bandgap (≈3.6 eV) of α-IGZO only allows the absorption of ultraviolet light. Numerous attempts have been made to extend its spectral response to visible and near-infrared regions by forming sub-bandgap states or introducing an additional absorption layer like oxides, nanostructures, chalcogenides, organic materials, perovskites, and nanodots to form a heterojunction structure with α-IGZO as the active layer [27]. Recently, hydrogen doping has been used to generate sub-bandgap states in the α-IGZO film to enable wide-spectrum visible light detection and boost its electrical performance, see Figure 2.2 [28]. Here in this thesis, upconversion nanoparticles (UCNPs) were used to further extend the spectral response of the hydrogen doped α-IGZO phototransistors (α-IGZO: H TFTs) to the near-infrared region with a high SNR.

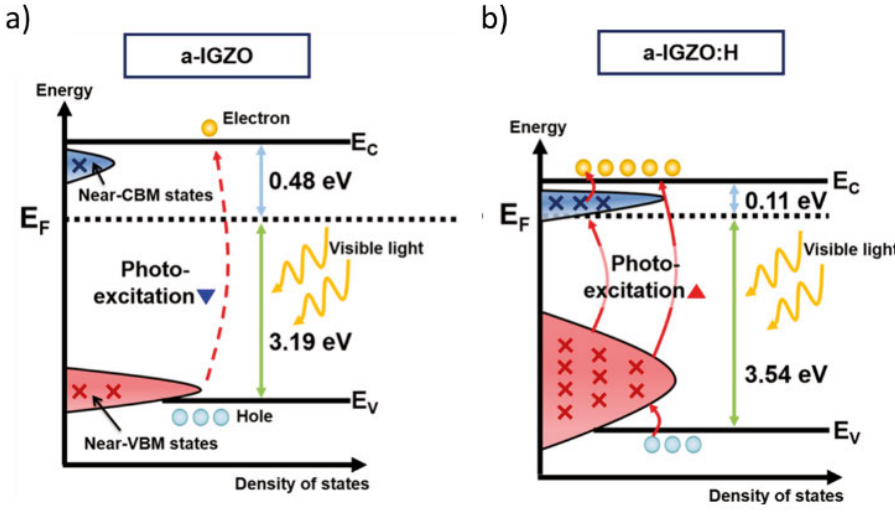

Figure 2.2 Schematic diagrams of the energy bands of (a) α-IGZO and (b) α-IGZO: H. Reproduced from [28] with permissions. Copyright © 2018, American Chemical Society

2.2 Upconversion nanoparticles

Fluorescence-based studies have been widely applied to biosensing and imaging due to their high sensitivity. Conventional fluorophores include organic dyes, fluorescent proteins, and QDs. Upconversion nanoparticles, as a novel fluorophore, have many advantages over other fluorophores including anti-Stokes shift, narrow and size-independent emission peak, good biocompatibility, high penetration depth into tissues, and high photostability [29]. The anti-Stokes shift is the most unique property of UCNPs, which means that the emitted ultraviolet or visible light has a shorter wavelength, *i.e.* higher energy, than the near-infrared excitation light. The NIR excitation could penetrate

deep with low adverse side effects on tissues and have virtually zero autofluorescence, which gives a high SNR for sensing and imaging. For the commonly used lanthanide-based UCNPs ($NaYF_4$:Yb, Er or $NaYF_4$:Yb, Tm), this unique property comes from the internal ladder-like energy levels with similar intervals and the metastable excited states of the lanthanide dopants such as Er^{3+} or Tm^{3+} as activators, which receive nonradiative energy transfer from neighboring sensitizers Yb^{3+} within the crystal host lattice $NaYF_4$ [30], as Figure 2.3a shows. Moreover, the mature surface chemistry technique can functionalize the surface of UCNPs with various molecules [31]. The diameter of commercially available lanthanide UCNPs with surface conjugates can range from micrometers to 30 nm with a narrow size distribution. Core-shell type UCNPs offer further advantages of reduced emission loss due to surface quenching [32]. In our studies, we have used commercial colloidal core-shell lanthanide-doped UCNPs ($NaYF_4$@$NaYF_4$: Yb, Er, and $NaYF_4$@$NaYF_4$: Yb, Tm) with surface conjugation of streptavidin or biotin and 30–40 nm in diameter, see Figure 2.3b-c. They have an excitation peak at 980 nm and emission peaks around 550 nm/650 nm for Er^{3+} doping and 350 nm/450 nm for Tm^{3+} doping, respectively, see Figure 2.3d-e. We choose these tiny UCNPs to aim at SMD.

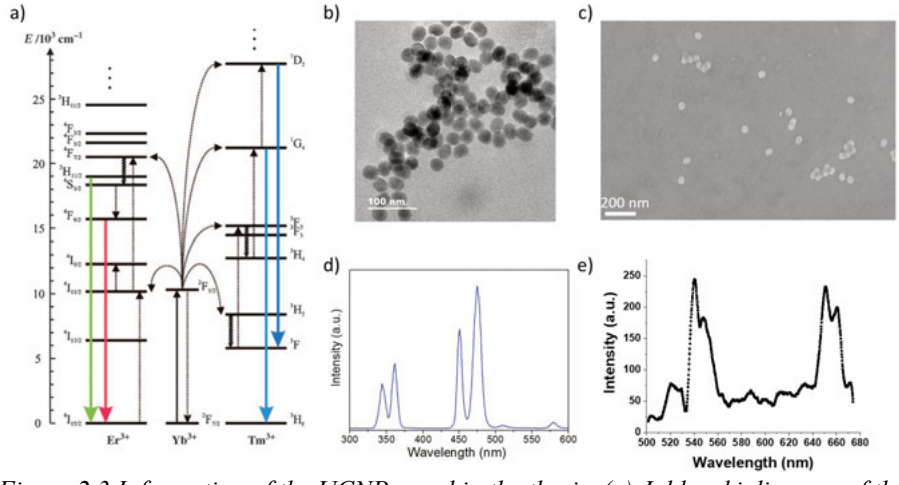

Figure 2.3 Information of the UCNPs used in the thesis. (a) Jablonski diagram of the lanthanide-doped UCNPs. Reproduced from reference [33] with permissions. Copyright © 2004 WILEY-VCH Verlag GmbH & Co. KGaA, Weinheim. (b) TEM graph and (c) SEM image of the UCNPs used in the thesis. (d) Emission spectra of the UCNPs $NaYF_4$: Yb, Tm. (e) Emission spectrum of the UCNPs $NaYF_4$: Yb, Er. (b) and (d) are provided by the RuixiBiotech company, China).

For single UCNP fluorescence imaging, its intensity is highly dependent on the excitation power density due to its non-linear optical process, and for sub-50 nm single UCNPs, it usually requires at least 10^4 W/cm^2 power density to be detected [34]. Normally, scanning confocal microscopes and widefield microscopes equipped with suitable laser sources can image single UCNPs. In

our studies, we have used both kinds of microscopes for fluorescence imaging of single UCNPs. The scanning confocal microscope has a Ti: Sapphire pulsed laser with a tunable wavelength from 650 nm to 1100 nm. The widefield microscope is equipped with a continuous-wave 980 nm diode laser. The photoluminescence (PL) intensity of a single UCNP ($NaYF_4$@$NaYF_4$: Yb, Er) we purchased exhibits a non-linear relationship with power density, see Figure 2.4a–b. At low power densities, below 2.0×10^5 W/cm^2, the PL intensity of the UCNPs increases exponentially with power density. However, at high power densities, above 2.0×10^6 W/cm^2, the PL intensity saturates, represented by a gradual plateau as the power density continues to increase. The photostability of the single UCNP is shown in Figure 2.4c. A typical PL image of a single UCNP detected by a commercial CCD camera is shown in Figure 2.4d.

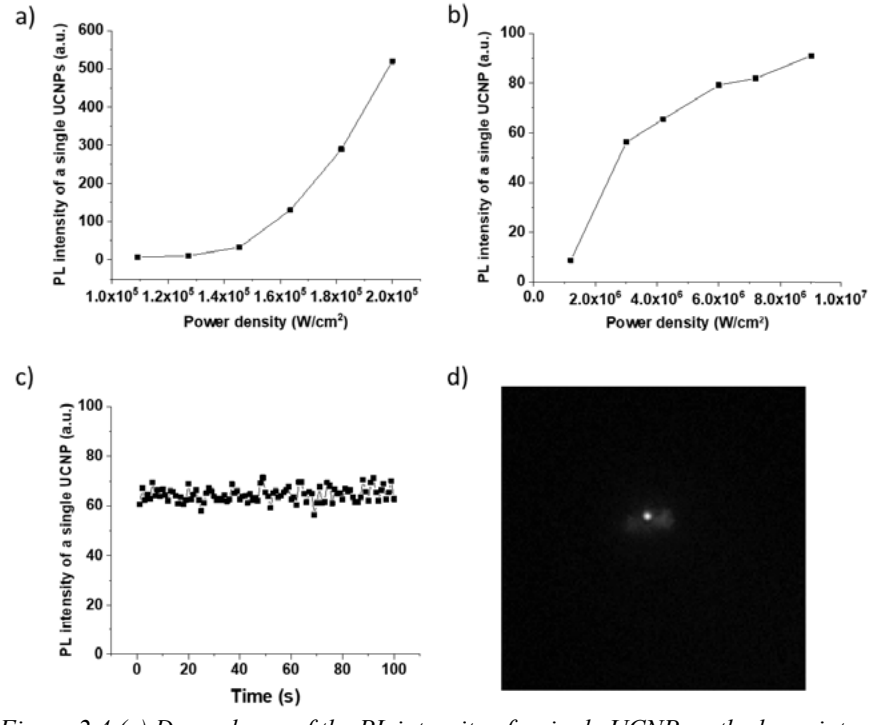

Figure 2.4 (a) Dependence of the PL intensity of a single UCNP on the laser intensity under the illumination from a 980 nm diode laser. (b) Dependence of the PL intensity of a single UCNP on the laser intensity under the illumination from a 980 nm pulsed laser (c) Times series of the PL intensity of a single UCNP, indicating its photostability. (d) A PL image of a single UCNP sitting on a bare glass substrate.

2.3 Förster resonance energy transfer

Förster resonance energy transfer (FRET) describes the physical process in which energy is nonradiatively transferred from an excited fluorophore (the donor) to another ground-state fluorophore (the acceptor) or quencher when approximate spectral overlap and proximity requirements are satisfied [35], see Figure 2.5a and c. The FRET efficiency is inversely proportional to the distance between the donor and the acceptor to the power of 6, which is usually within 10 nm, due to the dipole-dipole coupling [35]. Due to its high distance sensitivity on the nanometer scale, it is also called "molecular ruler", see Figure 2.5b [16]. The FRET efficiency can be measured either by the ratio of the donor's quantum yield, fluorescence intensity, and lifetime with and without the acceptor or by the fluorescence intensity enhancement of the acceptor with and without the donor under the excitation light for the donor. Ever since its first identification in the 1920s and verification in the 1960s, FRET has been widely applied to biosensing and imaging. Various bio-analytes such as DNAs, RNAs, proteins, enzymes, small molecules, viruses, and so on have been demonstrated to be detectable via FRET [36]. To detect biomolecules with ultrahigh sensitivity, to provide the distribution of a heterogenous population, and to unravel structural and mechanistic details, smFRET was experimentally achieved in 1996 and widely investigated since then due to the development of fluorescence spectroscopy and microscopy [14].

Our ensemble FRET measurement of classic FRET pair Cy3 and Cy5 by fluorescence spectroscopy is shown in Figure 2.5d. All the fluorescence emission spectra were measured by a Raman spectroscopy with a 532 nm laser, around the excitation peak of Cy3. Cy3 was conjugated with streptavidin (SA) and Cy5 was conjugated with biotin. The strong affinity between SA and biotin brought Cy3 and Cy5 close together for FRET. As Figure 2.5d shows, the Cy5 peak around 670 nm became obvious only when Cy3-SA and Cy5-biotin were mixed (black curve). The reference samples included Cy3-SA only (red curve), Cy5-biotin only (blue curve), and a mixture of Cy3-SA and Cy5-SA (green). The contributions to the FL intensity around 670 nm arise from the tail of Cy3 emission, the direct excitation of Cy5 by 532 nm laser, and the radiative energy transfer between Cy3 and Cy5 were limited. FRET contributed most to the 670 nm peak. Besides, the decrease of Cy3 FL intensity (around the 560 nm peak) was also observed, as expected by the FRET theory.

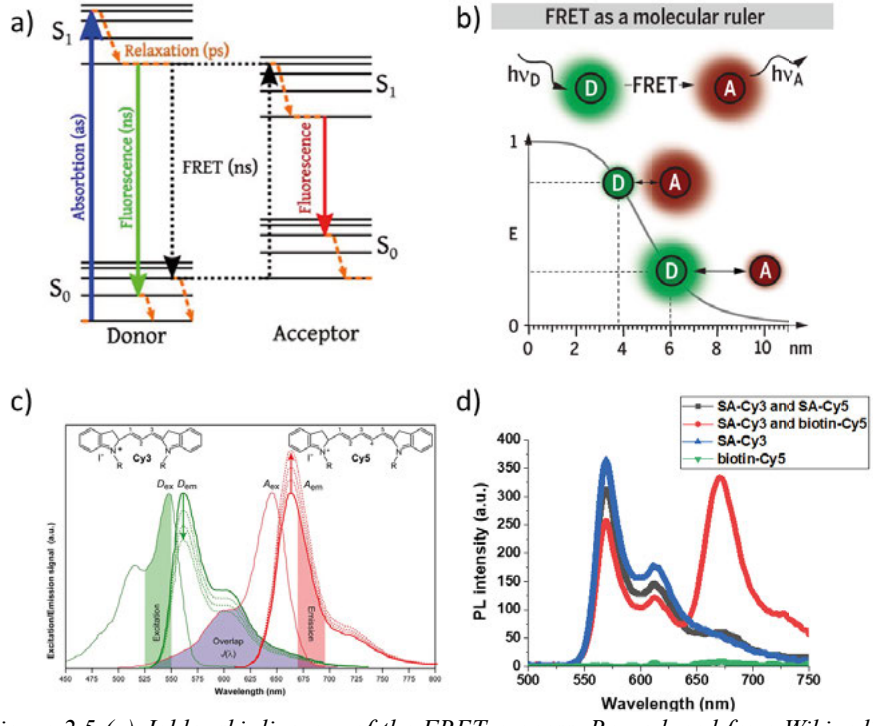

Figure 2.5 (a) Jablonski diagram of the FRET process. Reproduced from Wikipedia (https://en.wikipedia.org/wiki/F%C3%B6rster_resonance_energy_transfer). (b) Schematic showing the dependence of FRET efficiency on the distance between a donor and an acceptor, usually within 10 nm. Reproduced from [16] with permissions from AAAS. Copyright © 2018 The Authors. (c) Excitation and emission spectra of Cy3 and Cy5 molecules. Reproduced from [37] with permissions. Copyrights © 2012 The Authors. (d) Our ensemble FRET measurements of the Cy3-Cy5 FRET pair by spectroscopy.

In addition to the ensemble FRET measurements by spectroscopy, FRET imaging based on nanoparticles including QDs, UCNPs, and gold NPs by different kinds of fluorescence microscopes is also demonstrated in this thesis. The QDs and UCNPs are more photostable than organic dyes and have narrow emission peaks, which makes cross-talk ignorable in FRET measurements. In addition, their emission peaks can be tuned by changing their sizes or dopants. Fluorescence images of FRET pairs QDs-Cy5 and UCNPs-Cy5 are shown in Figure 2.6. . The scanning confocal microscope equipped with a Ti: Sapphire pulsed laser was used for this FL imaging. Both QDs and UCNPs were conjugated with streptavidin and immobilized on biotin-PLL functionalized glass substrates, and then Cy5-biotin was captured via the streptavidin-biotin interaction. The emission peaks of QDs and UCNPs are around 585 nm and 550 nm/650 nm, respectively. Both peaks overlap with the excitation spectrum of Cy5 and have ignorable crosstalk in the Cy5 emission channel with a 700 nm long-pass detection filter. Neither the 405 nm nor the 980 nm excitation light

source can excite Cy5, so the detected Cy5 signals could only result from FRET, as the schematics in Figure 2.6c and f show.

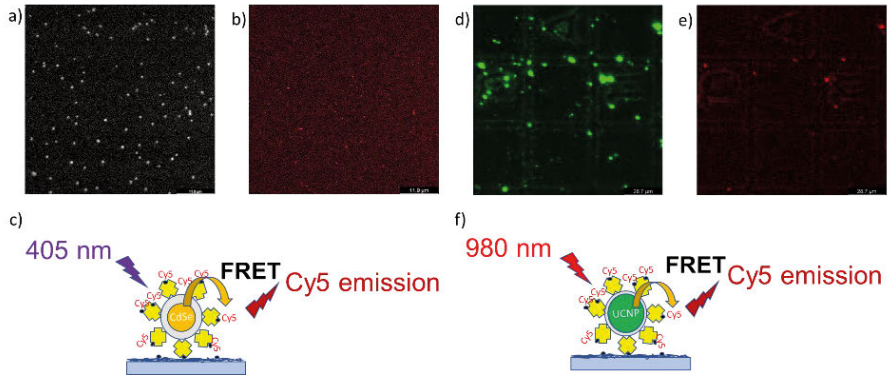

Figure 2.6 FRET imaging of QDs-Cy5 and UCNPs-Cy5 FRET pairs. Fluorescence images of (a) QDs and (b) Cy5 under 405 nm excitation light with a schematic (c). Fluorescence images of (d) UCNPs and (e) Cy5 under 980 nm excitation light with a schematic (f). Both QDs and UCNPs were conjugated with streptavidin (the yellow crosses) and immobilized on a biotin-PLL functionalized glass substrate. Image sizes are 50 µm × 50 µm for (a) and (b), 110 µm × 110 µm for (c) and (d).

Single nanoparticle-based FRET imaging could have high sensitivity for biosensing. Besides fluorophores, quenchers like Au NPs can also be the acceptor in FRET. Here, small gold NPs (1.8 nm in diameter) were demonstrated to quench PL from single UCNPs. The single UCNPs-SA were immobilized on the biotin-mPEG-silane functionalized SiO_2-Si substrates and biotin-Au NPs were captured by the UCNPs-SA, see Figure 2.7a. Streptavidin-biotin chemistry was also used here to bring the donor (UCNPs) and the quencher (Au NPs) close together, the latter of which has a wide absorption in the visible region, overlapping the emission peaks of the UCNPs. With increasing number of Au NPs (0.6 µM in concentration), the FL intensity of UCNPs continuously decreased, as the series of FL images in Figure 2.7b shows (from left to right, view size 106 µm × 106 µm, detection range 522–571 nm). Zoom-in scanned FL images (view size 21 µm × 21 µm) are depicted in Figure 2.7c. The first and second rows correspond to images of UCNPs only (Figure 2.7c i-iii) and UCNPs with Au NPs (Figure 2.7c iv-vi), respectively. The images from left to right correspond to the 522–571 nm, 639–678 nm, and combined detection channel. The SEM image of the same area after adding Au NPs and washing is shown in Figure 2.7d. The UCNPs in the SEM image are labeled with red and black circles, which correlate very well with the FL images (Figure 2.7). Au NPs partially quenched the ones with red circles and completely quenched the ones with black circles. The Au NPs conjugated on the single UCNP can be seen under SEM, see Figure 2.7e.

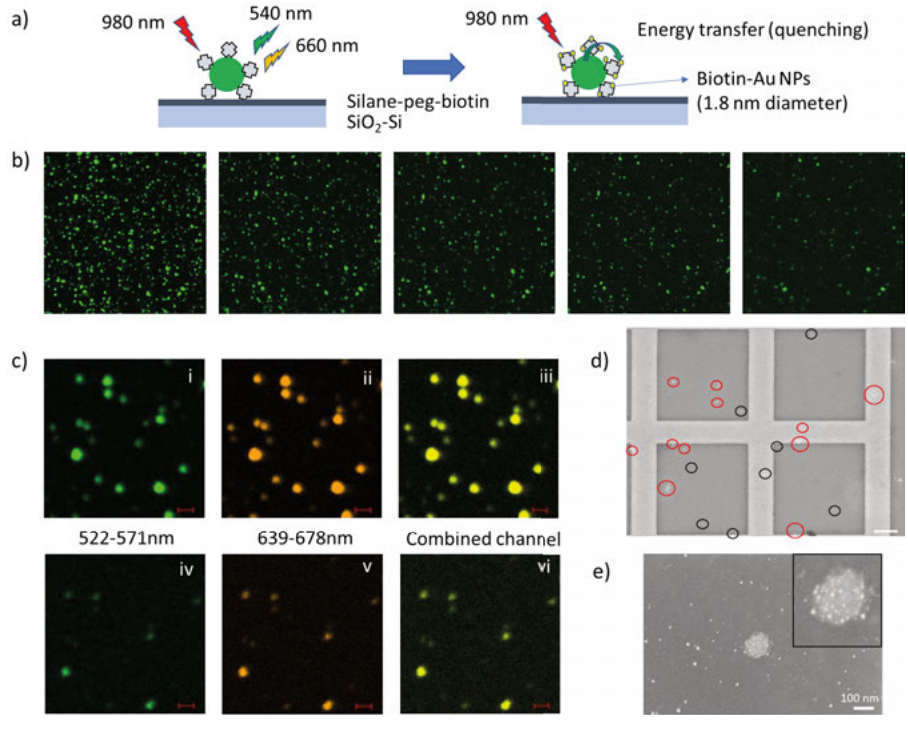

Figure 2.7 (a) Schematic of quenching UCNPs with AuNPs. (b) Fluorescence images of UCNPs show a decrease in FL intensity (from left to right) with gradually AuNPs adding, view sizes are 106 μm × 106 μm. (c) Zoom-in FL images of UCNPs before and after adding Au NPs in different detection channels, view sizes are 21 μm × 21 μm. (d) SEM image of the UCNPs in the same area as in (c). (e) An SEM image with a zoom-in inset at the upper-right corner to show the Au NPs conjugated on a single UCNP.

2.4 Plasmon-enhanced fluorescence

Plasmonics are well-understood physical phenomena related to the resonant oscillation of electrons in metallic nanoparticles or propagation along the metal-dielectric interface under light (electromagnetic EM wave) excitation and has been widely explored for myriad of applications [38]. Various metallic or dielectric nanostructures including nanorods, nanoparticles, nanopillars, nanogratings, nanoantenna, nanoholes, and nanohole arrays have been investigated to have surface plasmons in wide wavelength ranges from ultraviolet to near-infrared [39]. Both the localized surface plasmons (LSPs) from individual metallic nanoparticles and the surface plasmon polaritons (SPPs) from periodic nanostructures in a continuous metal film can strongly confine the electric field in the subwavelength volume [38]. The largely enhanced local electric field could significantly change the optical environment of the

adjacent fluorophores, both the excitation and emission processes of which can be affected [40], see Figure 2.8a. The observed fluorescence intensity can be described by:

$$I = \gamma_{\mathrm{ex}} \cdot \eta_{\mathrm{f}} \cdot \varepsilon_{\mathrm{coll}} \tag{3}$$

, where γ_{ex} is the excitation rate of the fluorophore, η_{f} is the emission quantum yield of the fluorophore, and $\varepsilon_{\mathrm{coll}}$ is the light collection efficiency of the optical system [41]. With plasmonic structures, equation (3) can be rewritten as:

$$I = \gamma'_{\mathrm{ex}} \left(\frac{\gamma'_{f,\mathrm{r}}}{\gamma'_{f,\mathrm{r}} + \gamma'_{f,\mathrm{nr}} + \gamma'_{f,\mathrm{ET}}} + \frac{\gamma'_{f,\mathrm{ET}}}{\gamma'_{f,\mathrm{r}} + \gamma'_{f,\mathrm{nr}} + \gamma'_{f,\mathrm{ET}}} \cdot \frac{C_{\mathrm{scat}}}{C_{\mathrm{abs}} + C_{\mathrm{scat}}} \right) \varepsilon_{\mathrm{coll}} \tag{4}$$

- γ'_{ex} is the increased excitation rate.
- $\gamma'_{f,\mathrm{r}}$ is the modified radiative decay rate of the fluorophore.
- $\gamma'_{f,\mathrm{nr}}$ is the modified nonradiative decay rate of the fluorophore.
- $\gamma'_{f,\mathrm{ET}}$ is the energy transfer rate from the fluorophore to the plasmonic nanostructure.
- C_{abs} is the absorption cross section of the plasmonic nanostructure.
- C_{scat} is the scattering cross section of the plasmonic nanostructure.

By optimizing the dimensions of nanostructures and the positions of the fluorophores, large fluorescence intensity enhancement has been achieved [42]. For lanthanide-doped single UCNPs, the fluorescence enhancement factor by plasmonic nanostructures could reach a phenomenal number of 2.3 $\times 10^5$, see Figure 2.8b [43], [44].

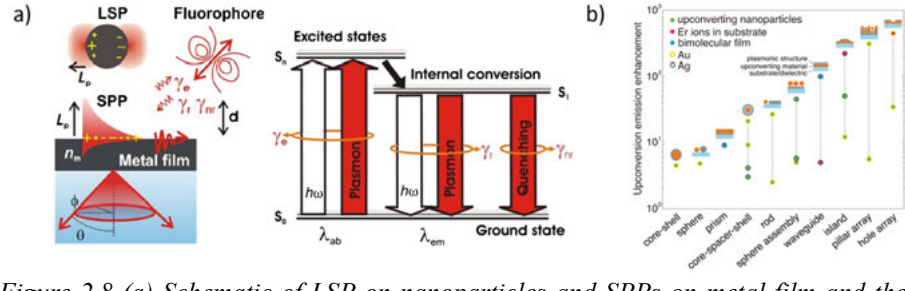

Figure 2.8 (a) Schematic of LSP on nanoparticles and SPPs on metal film and the effect of plasmon on the fluorophore transitions between ground state and excited states. Reproduced from [40] with permissions. Copyright © 2013, Springer Science Business Media New York. (b) Large fluorescence enhancement factors by typically used plasmonic nanostructures for some frequently studied UCNPs. Reproduced from [43] with permissions, Copyright © 2014, American Chemical Society.

3 Amorphous InGaZnO: H-based Phototransistors

3.1 Fabrication and electrical characterization of α -IGZO:H TFTs

The α -IGZO:H-based phototransistors (IGZO:H-TFTs) were fabricated with standard silicon technology, see Figure 3.1. A 120 nm-thick oxide layer was thermally grown on a heavily boron-doped silicon wafer. The substrate was later used as the back gate and the oxide layer as the gate insulator. A 40 nm-thick α -IGZO:H active layer was then sputter-deposited on the front surface of the wafer with a mixed Ar and H_2 plasma ($\frac{H_2}{H_2+Ar} = 2\%$) [28]. The IGZO target was composed of In_2O_3/Ga_2O_3/ZnO at 1:1:1 ratio. The hydrogen doping creates sub-bandgap states in α -IGZO, which expands the visible light detection range of α -IGZO from ultraviolet [28]. Post-annealing was conducted at 200 °C in air for 20 min. Next, metal stack comprising a 40 nm-thick Au on top of a 5 nm-thick Cr glue layer forming the source and drain electrodes was fabricated on top of the IGZO thin film by combining EBL, evaporation, and lift-off processes.

Figure 3.1 Schematic of the main fabrication processes of IGZO:H-TFTs.

The layout of the electrodes on an 8 mm × 8 mm chip is depicted in Figure 3.2a.

There were 30 devices in total on each chip with different submicron lengths and widths between the source and drain electrodes. A central signal line was used as the common drain of all the devices in order to optimize the device design and to ease the subsequent optoelectronic characterization. Then, a 100 nm-thick aluminium layer was sputter-deposited on the backside of the wafer. After slicing the wafer into 8 mm × 8 mm chips, the edges of the chips were wet-etched by dipping into diluted HCl solution to avoid direct contact between the IGZO layer and the substrate back-gate. Thereafter, a 30 nm-thick Al_2O_3 layer was deposited on the central part of the chip by means

of ALD. A coverslip with a 6 mm-diameter hole drilled in the central area was used as the shadow mask for ALD, see Figure 3.2b-c. A cross-sectional schematic of the IGZO:H-TFT is presented in Figure 3.2d. The Al_2O_3 passivation layer on top of the IGZO:H active layer could enhance the electrical stability of the devices both in air and in liquid [45], [46], see Figure 3.2g–i. An IGZO:H-TFT with a gap of 500 nm × 500 nm between the source and drain electrodes was measured in air and in dark to extract electrical parameters from the output and transfer characteristics displayed in Figure 3.2e-f, respectively. It was characterized by a maximum on-to-off current ratio (I_{on}/I_{off}) of 10^9, a subthreshold swing (*SS*) of 0.3 V/decade, threshold voltage (V_{th}) of +2.0 V, and saturation mobility (μ_{sat}) of 31 cm^2/Vs. The large *SS* and V_{th} values mainly result from the very thick back SiO_2 gate dielectric used [47]. The electrical measurements here were performed on a probe station connected to a semiconductor parameter analyzer Agilent (B1500A).

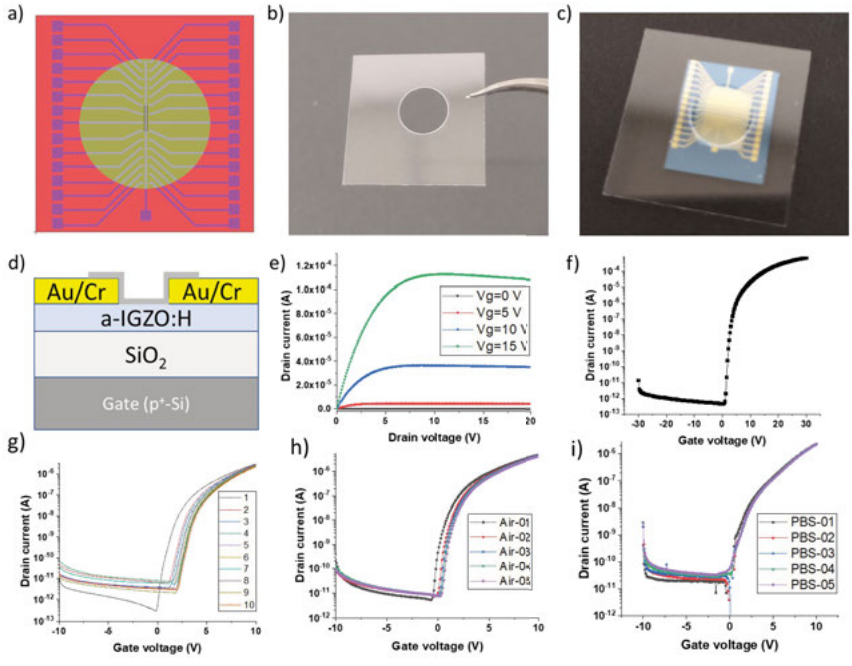

Figure 3.2 (a) Designed pattern of the phototransistors on an 8 mm × 8 mm chip. The central circle was left for the Al2O3 passivation layer deposition. (b) A 170 µm-thick coverslip with a 6 mm-diameter hole was used as the mask for Al2O3 deposition. The hole was drilled by a laser cutter. (c) The fabricated chip with the coverslip on top for Al2O3 deposition. (d) Schematic of the IGZO:H-TFT device with an Al2O3 passivation layer. (e) Output characteristics of an IGZO:H-TFT with different gate voltages. (f) Transfer characteristic of the same device measured in (e), source-drain voltage was fixed at 10 V. (g) Transfer curves of an IGZO:H-TFT measured in air without the Al2O3 passivation layer. Gate voltage was swept from –10 V to +10 V consecutively for ten times. (h) Transfer curves of an IGZO:H-TFT in air but with the Al2O3 passivation layer. The device had the same dimensions as the device in (g). Gate voltage was swept consecutively for five times. (i) Transfer curves of another IGZO:H-TFT in 1X PBS solution with the Al2O3 passivation layer. The device had the same dimensions as the device in (g) and (h). Gate voltage was swept from –10 V to +10 V consecutively for five times.

3.2 Molecular sensing with UCNPs and FRET

The visible light detection ability of the IGZO:H-TFTs was first confirmed on the probe station. A 532 nm diode laser was mounted on the probe station, see Figure 3.3a–c. The laser was focused on the devices by the objectives. The transfer curves of the devices were measured in dark, with light on and then light off, see Figure 3.3d–f. It shows that the 532 nm green light could generate photocurrent in the IGZO:H-TFTs, validating that the hydrogen doping could

expand the visible light detection of IGZO. The laser power was fixed, while the light intensity could be altered by changing the objectives. The higher the light intensity, the higher photocurrent was with a fixed gate bias around +5 V, see Figure 3.3.f.

The chip was carefully wire-bonded onto a chip holder with silver paste and Au wires. Good electrical contacts between the metallic substrate of the chip holder and the heavily-doped substrate of the chip were assured by the silver paste for providing the gate bias. The chip holder was previously soldered onto a custom-designed PCB, see Figure 3.3a. To capture and immobilize the SA-UCNPs on top of the IGZO:H active layer between the source and drain electrodes, the surface of the Al_2O_3 passivation layer was functionalized with PLL-g-PEG-biotin (PPB), which was adhered to the Al_2O_3 by electrostatic force [48]. A PDMS well was mounted on top of the chip for solution loading. After the surface functionalization, the colloidal SA-UCNPs could be immobilized on the surface. Some SA-UCNPs were captured at the submicron-sized gap between the source and drain electrodes, see Figure 3.4d. Due to the convection and diffusion-based loading method, both the SA-UCNP concentration and volume were optimized to have a few SA-UCNPs at the submicron gap between the source and drain electrodes. As control samples, the devices without the PPB functionalization had very few SA-UCNPs immobilized after identical incubation and washing steps, see the comparison between the top-view SEM images of two devices in Figure 3.4b–c. There were always SA-UCNPs captured outside the gap between the source and drain electrodes. However, the Synopsys Sentaurus TCAD simulation result indicated that the current mainly flows between the source and drain electrodes with very limited lateral expansion, *i.e.* at 100 nm away in perpendicular to the current flow direction, the current density is a factor of e lower than its highest value along the central line of the channel, as Figure 3.4e shows. Thus, the emitted fluorescence light from the SA-UCNPs outside the gap may contribute little to the photocurrent considering the near-zero radiation angle, and only the SA-UCNPs at the gap matter.

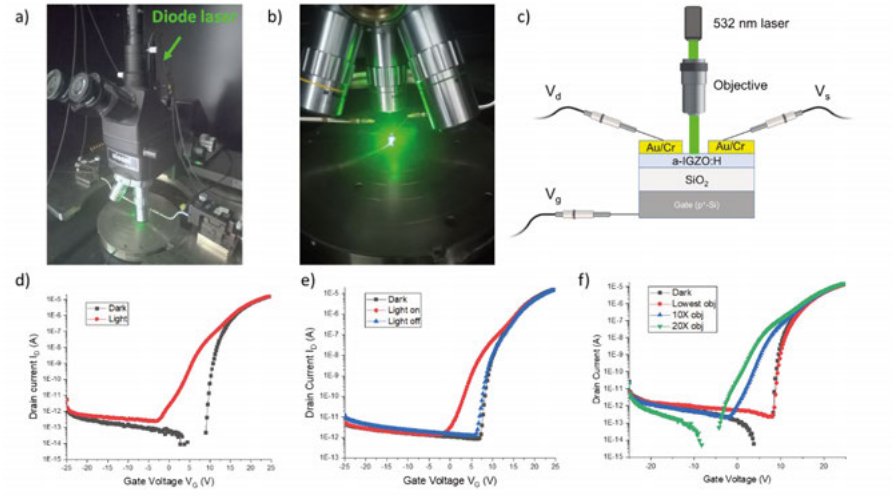

Figure 3.3 (a) Experimental setup of a green diode laser mounted onto the probe station. (b) The laser was focused on the device by an objective, and probes were connected to the electrodes of the device. (c) Schematic of the setup in (b). (d) Transfer characteristics of an IGZO:H-TFT measured in dark and with light on. The channel was 1 µm in length and 100 nm in width. (e) Transfer characteristics of another IGZO:H-TFT measured in dark, with light on, and with light turned off. The channel was 500 nm in length and 100 nm in width. (f) Transfer characteristics of another IGZO:H-TFT measured in dark, and with light illumination of different intensities by changing magnification of the objective (the lowest magnification is 5X).

The sub-50 nm UCNPs usually require a high laser power intensity to excite [34], and it is nontrivial to confirm if the fluorescence signals are from the small UCNPs. To make sure that there were excited SA-UCNPs between the source and drain electrodes, a fluorescence microscope was integrated with the electrical measurement system for the optoelectronic characterization, see Figure 3.5a. The fluorescence microscope mainly consisted of a 980 nm continuous-wave laser, an objective (100X, 0.73NA), optical filter sets, an EMCCD detector, and a spectrometer. The electrical measurement system consisted of the chip wire-bonded on a chip-holder on a custom-designed PCB and a semiconductor parameter analyzer (Hewlett Packard 4155A). A white LED was used to align the laser beam with the IGZO:H-TFTs. The focused 980 nm laser through the objective lens could provide sufficient power intensity to excite the SA-UCNPs. The photoluminescence signals of the excited SA-UCNPs were detected by both the EMCCD detector and the fabricated IGZO:H-TFT. Moreover, the spectrometer could measure the emission spectrum of the UCNPs. The measured characteristic emission peaks of the UCNPs confirmed that the detected signals were from the UCNPs.

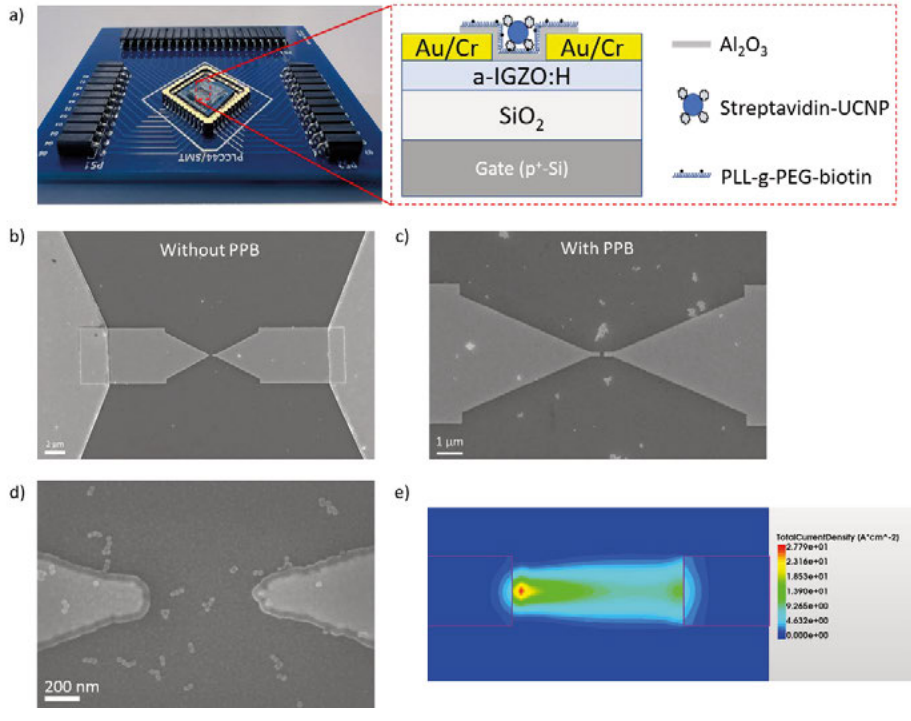

Figure 3.4 (a) A photo of a chip mounted onto a chip-holder on a custom-designed PCB. A PDMS well was mounted on top of the chip for surface functionalization and capturing SA-UCNPs. (b) A top-view SEM image of a device without PPB functionalization after incubating SA-UCNPs solution and washing. (c) A top-view SEM image of another device with PPB functionalization after incubating SA-UCNPs solution and washing. (d) A top-view SEM image of a device with PPB functionalization and many SA-UCNPs between the source and drain electrodes. (e) TCAD simulation of current density distribution between the source and drain electrodes from top-view. It has the same dimensions as the device in (d).

The bandgap of the IGZO:H is higher than the photon energy of the NIR light but smaller than the photon energy of the UV-visible light from the UCNPs. Thus, the UV-visible light emitted from the UCNPs generated electron-hole pairs (EHPs) in the IGZO:H active layer, thus, increases the photocurrent [28]. But the 980 nm light was insufficient to generate any photocurrent (by comparing the black and red curves in Figure 3.5b). For the device without PPB functionalization and measured in dark, the shape of the transfer curve was modified after adding the SA-UCNPs (by comparing the blue and black curves in Figure 3.5b), which was probably due to the surface adsorption of ions in the electrolyte causing change of the surface potential of the IGZO:H channel. Without PPB functionalization, there were few UCNPs staying at the gap but not immobilized, limiting the photo-response as well as the further FRET-based characterization. An expected parallel negative shift of V_{th} was observed due to the photogating effect (see the green and blue curves in Figure 3.5b.

After surface-functionalizing another IGZO:H-TFT with PPB to enhance the immobilization of SA-UCNPs, a much stronger photo-response was observed under the illumination of the 980 nm laser (comparing the black and green curves in Figure 3.5c). The significantly larger concentration of generated EHPs also contributed to an enhanced channel conductivity due to photoconductive effect in addition to a V_{th} shift. Around 100 UCNPs were found at the gap between the source and drain of the device, and the photocurrent on/off ratio was around 10^5. A simplified estimate from these data indicated that each UCNP may have a photocurrent-to-dark current ratio of 10^3. After adding biotin-AuNPs, the photocurrent dropped back to the original level, thus validating the FRET-based quenching effect on the chip (see the green and blue curves in Figure 3.5c). Each SA-UCNP could at the most capture 100 biotin-AuNPs, then each biotin-AuNP may cause one order of magnitude decrease of the photocurrent, which is promising for single-molecule detection. The initial V_{th} difference between the two devices in Figure 3.5b–c was most probably due to the charge of the PPB [48], the time and intensity difference of the unavoidable white LED illumination while aligning the 980 nm laser beam with the channel.

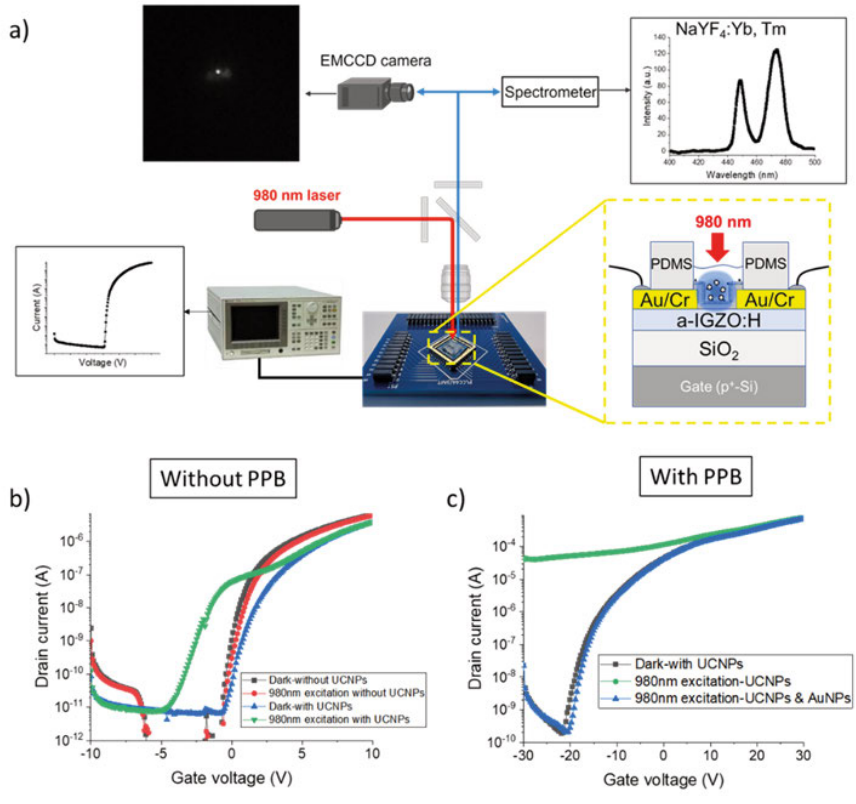

Figure 3.5 (a) Schematic of the integrated experimental setup for optoelectronic measurements that combines UCNPs and FRET on the IGZO:H-TFTs. (b) Transfer curves of an IGZO:H-TFT without PPB functionalization at different steps. (c) Transfer curves of another IGZO:H-TFT with PPB functionalization but with the same dimensions as the one in (b). The FRET-based detection is demonstrated in (c) by incorporating biotin-AuNPs. The two devices were measured both in dark and under 980 nm illumination.

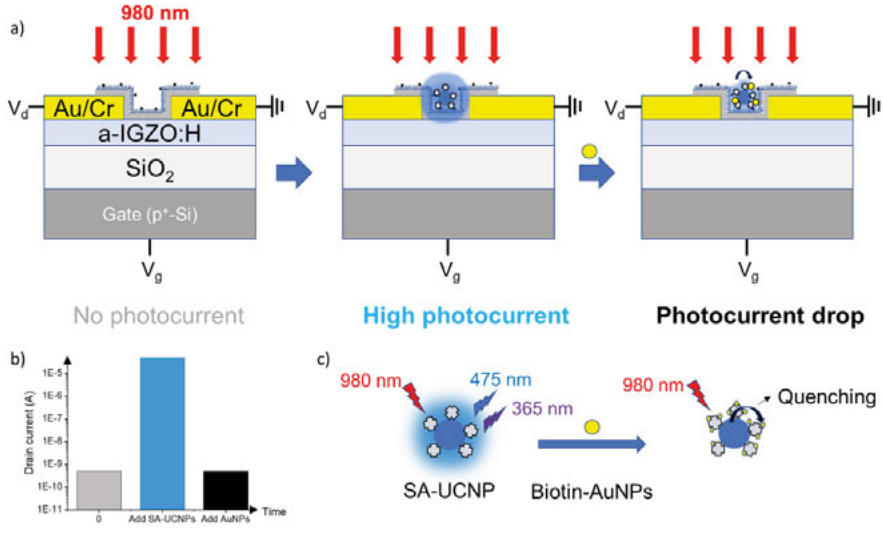

Figure 3.6 (a) Schematic of the steps for detecting the FRET-based quenching effect by monitoring the photocurrent change of the IGZO:H-TFTs. SA-UCNPs and biotin-AuNPs are integrated with the IGZO:H-TFTs. (b) A histogram to show the photocurrent changes in the timeline of experiments. (c) Schematic of the FRET-based quenching effect of SA-UCNPs caused by the biotin-AuNPs.

To better illustrate the main steps for demonstrating the detection of FRET-based quenching effect on the IGZO:H-TFTs, schematics according to the three curves in Figure 3.5c are shown in Figure 3.6a. Briefly, before adding the SA-UCNPs, the 980 nm light generated no photocurrent. After adding the SA-UCNPs, the UV-visible light from the SA-UCNPs generated large photocurrent under the 980 nm light illumination. Then, after the biotin-AuNP addition, the SA-UCNPs were quenched via FRET and the photocurrent drops, see Figure 3.6.

Therefore, the IGZO:H-TFT-based optoelectronic sensor presents a platform for ultrasensitive biosensing by integrating UCNPs and FRET. The surface of UCNPs could be conjugated with various molecules, which could enable detection of various analytes like ions, DNA, and proteins, *etc.* via the FRET mechanism. It is also promising towards a portable and inexpensive single-molecule sensor system. Only a 980 nm CW diode laser with enough power density, a microfluidic delivery system, and an integrated circuit for both providing voltages and analysing electrical signals are needed for this sensor system.

3.3 Fabrication of α-IGZO:H nanowire-based transistors

Nanowire-based TFTs (NWTFTs) would offer ultrahigh sensitivity for biosensing due to their high surface-to-volume ratio and low dark-current [49]. IGZO:H NWTFTs were fabricated mainly with EBL and Cl-based dry-etching processes [50], see the schematics of the process flow in Figure 3.7a. Firstly, a thin layer of hexamethyldisilazane (HMDS) was deposited on the surface of the IGZO:H film to enhance the adhesion of the subsequently coated resist layer. A 600 nm-thick UVN 2300.05 negative resist layer was then spun on the surface. Next, after the pre-bake at 100℃ for 1 min, IGZO:H stripe patterns with 100 μm in length and 75 nm, 100 nm, 150 nm, 250 nm, 500 nm, and 1000 nm in width were written by EBL with dose 0.2~0.3 $\mathrm{C/m^2}$. Then, it was post-baked at 110℃ for 1 min, developed in the MF-CD26 developer for 1min, rinsed in DI water for 1min, and hard-baked at 110℃ for 2 min. After resist baking, the exposed IGZO:H was etched using ICP-RIE with a mixture gas flow of 30 sccm Cl_2 and 50 sccm BCl_3, at 6.0 mTorr pressure, 800 W power, and 80 W bias for 1 min. Subsequently, the residue resist was removed using the resist remover AR 600-71. Imaging with optical microscope and SEM confirmed the successfully fabricated IGZO nanowires, see Figure 3.7b–d. The IGZO nanowires with displacement in Figure 3.7b came from the UVN resist mask nanostripes before the etching. However, the adhesion between the UVN resist mask nanostripes and the IGZO film was poor. Consequently, the UVN resist mask nanostripes showed displacement after the development and washing steps, leading to the same displacement of IGZO nanowires after etching. In addition to the ICP-RIE etching, ion milling was also investigated to etch IGZO. However, the edges of the etched IGZO became rough after being physically bombarded by Ar^+, see the cross-section SEM image in Figure 3.7e. To make smaller IGZO nanowires, other negative resists like HSQ with a higher resolution and etching-resistance than the UVN 2300.05 resist, together with optimized dry etching are necessary [50]. The source and drain Au/Cr electrodes of the IGZO:H NWTFTs were made by means of EBL-lift-off process. Several electrode pairs with different gap lengths can be made on a single IGZO nanowire with 100 μm length as both NWTFTs and transmission line model test structures for extracting contact resistance, see Figure 3.8.

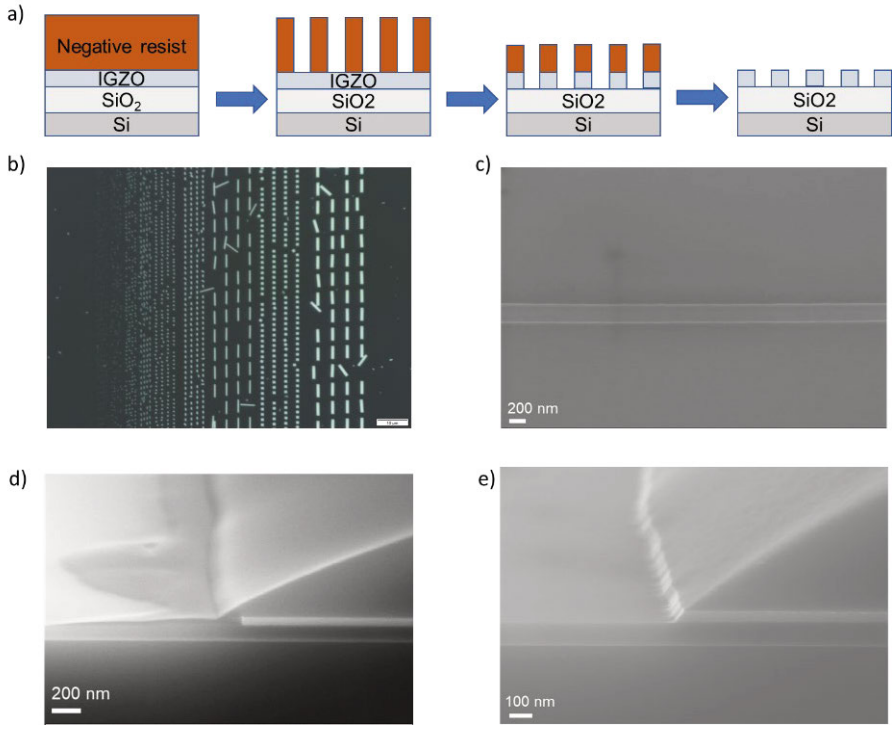

Figure 3.7 (a) Schematic of the processing flow for making IGZO:H nanowires. (b) An optical image of the fabricated IGZO wires with different widths and lengths. (c) A top-view SEM image of an IGZO wire with width around 250 nm. (d) A cross-section view SEM image of the IGZO:H film etched by ICP-RIE with the resist layer as mask. (e) A cross-section view SEM image of the IGZO:H film etched by ion milling with the resist layer as mask. Both images in (d) and (e) have a 10° tilt angle.

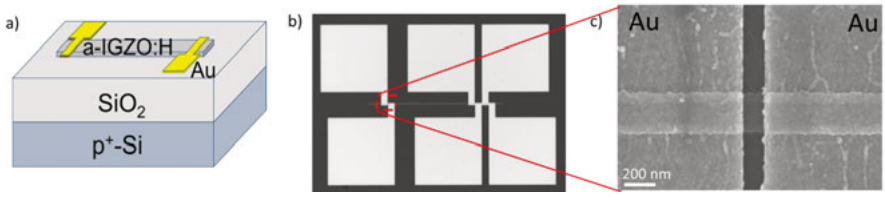

Figure 3.8 (a) Schematic of an IGZO:H-based NWTFT. (b) A top-view optical image of the fabricated IGZO:H-based NWTFTs on a single 100 μm-long IGZO:H nanowire. (c) A top-view SEM image of one of the devices in (b).

4 Plasmon-enhanced photoluminescence

For fluorescence-based biosensing and bioimaging, achieving a high SNR is crucial for high sensitivity and specificity. To enhance the SNR, one approach is to amplify fluorescence signals, while another is to reduce the background noise. Apart from selecting inherently bright fluorophores, the plasmonic properties of various metallic nanostructures have been explored to amplify the fluorescence signals via modifying the optical environment of the fluorophores. Additionally, plasmonic metal nanostructures, such as nanoholes in a thin metal film, can significantly limit the optical observation volume, thereby reducing background noise. The combined effects of signal enhancement and noise reduction make plasmonic nanostructures a promising approach for single-molecule detection through single fluorophore-based studies.

Specifically, nanoholes in a thin Al film can be divided into two classes: optically isolated zero-mode waveguides (ZMWs) and optically coupled nanohole arrays, primarily depending on the geometrical arrangements of the nanoholes. The optically coupled nanohole arrays exhibit a higher average electric field enhancement within the nanohole volume than ZMWs due to surface plasmon coupling, contributing to a higher fluorescence intensity enhancement factor.

The plasmon-enhanced photoluminescence of single quantum dots (QDs), molecular fluorophore-tagged single small extracellular vesicles (sEVs), and single UCNPs is systematically investigated in this Chapter. In the first two cases, the fluorophores (*i.e.*, QDs and fluorophore-tagged EVs) were immobilized in optically coupled nanohole arrays in a thin Al film. The former with QDs is mainly for fundamental understanding, while the latter with sEVs focuses on a specific application. The structural parameters of the nanohole arrays were designed and optimized via numerical simulations to achieve a plasmonic peak overlapping with the excitation wavelength. The nanohole arrays were fabricated on a glass substrate using magnetron-sputtering, electron-beam lithography (EBL), and dry etching with a precise control of the structural parameters. Colloidal single QDs and sEVs were immobilized in the nanoholes after surface functionalization. An epi-fluorescence microscope with illumination from the glass side, *i.e.* the rear side of the metallic film, was employed for fluorescence imaging. Only the fluorophores inside the nanoholes were detected from the glass side due to the presence of the opaque Al film blocking the fluorophores landing on the Al surface. Statistically, a five-

fold fluorescence intensity enhancement was achieved for single QDs based on their blinking behaviour (Paper I). An average 1.3-fold fluorescence intensity enhancement was achieved for molecular R-PE fluorophores tagged on single sEVs as well as a 12-fold increase in the number of detected sEVs (Paper II). Single UCNPs were site specificallyimmobilized in the gaps of gold nanorod dimers (GNRDs) using electron-beam induced deposition (EBID) technique. An overall 3-fold PL intensity enhancement was achieved.

4.1 Zero-mode waveguides

Zero-mode waveguides (ZMWs) are typical optically isolated subwavelength nanoholes in a thin metallic film. Zero-mode waveguides exhibit a cut-off wavelength above which no propagating modes exist within the waveguides, causing longer wavelengths to decay exponentially along the length of the waveguides and resulting in no transmission through the nanoholes [51]. A remarkable application of ZMWs is DNA sequencing by Pacific Biosciences [51]. The sub-diffraction-limit nearfield atto- to zepto-liter (1 zeptoliter = 10^{-21} L) effective observation volume within the waveguides enables single-molecule analysis at high biologically relevant concentrations (μM–mM) [52]. ZMWs can enhance the fluorescence intensity of fluorophores and also enhance FRET [53], [54].

In this thesis, ZMWs with diameters ranging from 50 to 200 nm and a period of 1 μm were fabricated in Al films of 50 and 100 nm thickness on glass substrates. The fabrication process is illustrated in Figure 4.1a. First, the Al film was sputter-deposited on a pre-cleaned coverslip glass substrate. Next, EBL was utilized to create nanoscale circular patterns in a spin-coated positive resist layer. Reactive-ion etching (RIE) with a Cl_2 and BCl_3 gas mixture then transferred the pattern into the Al film to form the desired ZMWs. Finally, residue resist was removed using a resist remover. A top-view SEM image of the fabricated ZMWs is shown in Figure 4.1d. A PDMS container with four 3 mm-diameter holes was mounted on top of the chip containing four nanohole arrays. Experimental solutions were loaded into the PDMS container, as illustrated in Figure 4.1b–c.

The fabricated Al ZMWs were surface-functionalized with poly(vinylpolypyrrolidone) (PVPA) and BSA-biotin to prevent nonspecific adsorption and to immobilize streptavidin-conjugated fluorophores at the bottom of the ZMWs, *i.e.* on the surface of the glass substrate, by benefiting from the streptavidin-biotin binding pair (Figure 4.1c). The excitation light from the epi-fluorescence microscope illuminated from the glass side, while the emitted fluorescence signals from the fluorophores at the bottom of the ZMWs were detected through the same optical path. Streptavidin-conjugated QDs were immobilized in an Al ZMW array with a 200 nm nanohole diameter, and streptavidin-Cy5 were immobilized in an Al ZMW array with a 150 nm

nanohole diameter. Both Al ZMW arrays had an Al thickness of 100 nm and a period of 1 µm. A 100% filling efficiency was achieved with a high concentration of fluorophores and, therefore, a high SNR was attained due to the opaque Al film, as shown in Figure 4.1e. The fluorescence intensity variation of the QDs inside the ZMWs was mainly due to the different number of QDs in each ZMW. However, for molecular Cy5 dyes, the size of which is too small, making the difference in the number of Cy5 negligible comparable to the total number of Cy5 molecules in each ZMW, resulting in nearly uniform fluorescence intensities of Cy5 in the ZMWs.

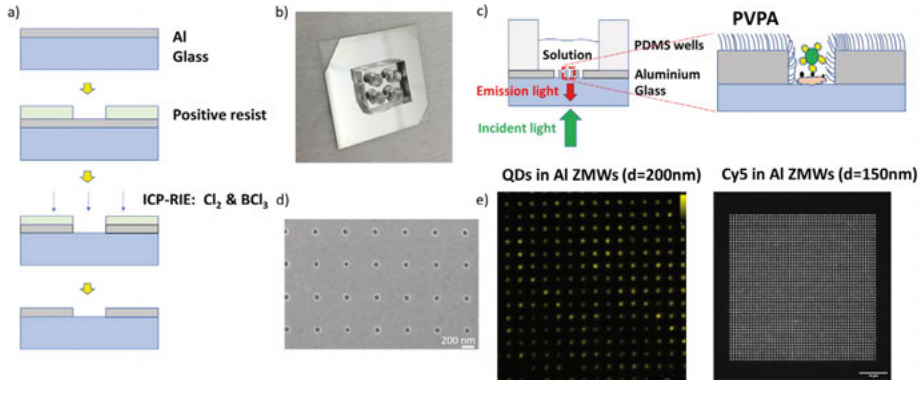

Figure 4.1 (a) Schematics of the processing flow for the fabrication of ZMWs. (b) A real chip with four ZMW arrays and PDMS wells on top of the Al film (front side). (c) Schematic device with the ZMWs and the measurement setup. Streptavidin-QDs were immobilized in the ZMWs by BSA-biotin. (d) A top-view SEM image of the fabricated ZMWs. (e) Fluorescence images of QDs in the 200 nm-diameter ZMWs and Cy5 in the 150 nm-diameter ZMWs. Both arrays were embedded in an Al film with a thickness of 100 nm and a period of 1 µm.

The simulated electric field distribution of a 100 nm thick Al ZMW versus a 50 nm thick Al ZMW in an aqueous environment is, respectively, shown in Figure 4.2a and c, both with a nanohole diameter of 50 nm. With 980 nm light incident from the glass side, the electric field intensity decays exponentially, as expected, along the central line inside the ZMW, as illustrated in Figure 4.2b and d. The electric field distribution inside the two types of Al ZMWs is similar. The 50 nm thick Al ZMWs requires less Al material and a lower aspect ratio for dry etching than for the 100 nm thick Al ZMWs with the same nanohole diameter. The electric field increases when the period of the ZMW array decreases from 1000 nm to 350 nm, caused by an increased optical plasmonic coupling between the ZMWs as the period decreases. However, the diffraction-limited resolution of an optical microscope, approximately half of the excitation wavelength, must be considered. If the period of the ZMW array is smaller than the resolution of the optical microscope, it could be challenging to distinguish the fluorescent spots from neighboring ZMWs.

Although optically isolated ZMWs have been used for single-molecule analysis, such as DNA sequencing [51], due to their tiny excitation volume and high SNR [55], they exhibit low fluorescence enhancement due to a relatively low electric field enhancement. Several methods have been attempted to enhance fluorescence intensity, such as over-etching the ZMWs or combining plasmonic nanoantenna with ZMWs [56], [57]. In this thesis, the electric field intensity in each nanohole is increased by simply decreasing the period of the nanohole array in order to utilize the plasmonic coupling between the nanoholes, thereby enhancing the fluorescence intensities of single fluorophores inside.

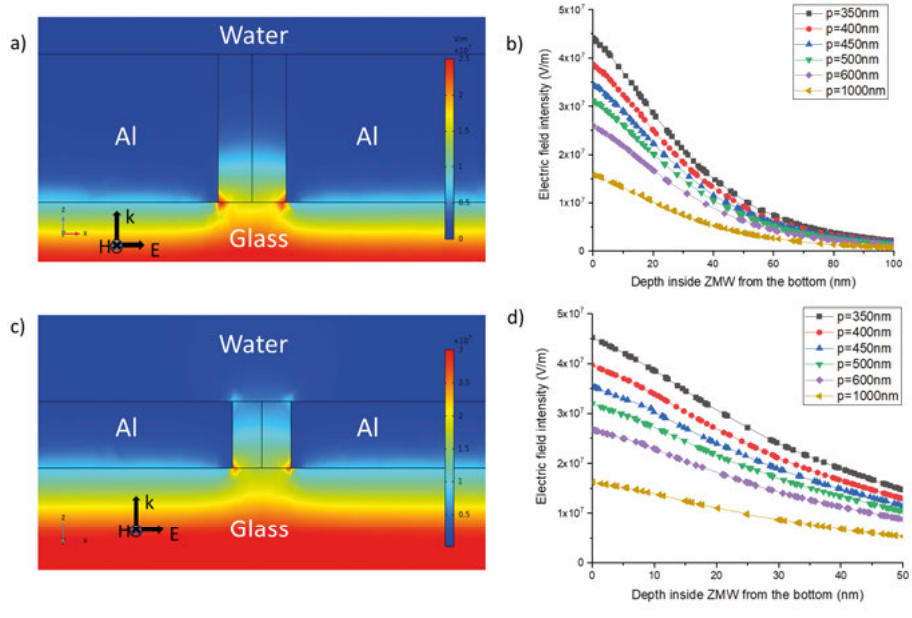

Figure 4.2 Simulation of electric field distribution inside an Al ZMW of 50 nm diameter and 100 nm (a–b) versus 50 nm thickness (c–d) under 980 nm excitation.

4.2 Plasmon-enhanced fluorescence of single QDs in Al nanoholes

Quantum dots (QDs) are semiconductor nanodots, typically several nanometers in diameter [58]. Due to the three-dimensional quantum confinement, QDs exhibit discrete, atom-like electronic structures with size-dependent energy levels. This characteristic enables widely tunable light absorption and narrowband emission across the visible and infrared spectra [59], making QDs highly versatile for applications in bioimaging, biosensing, energy harvesting, lasers, and quantum information systems [59]. Quantum dots can be

synthesized via both physical vacuum-based methods and chemical solution-phase processes, the latter of which produces colloidal QDs [59]. Advanced surface engineering techniques allow QDs to conjugate with various ligands and biomolecules, facilitating their use in biosensing and bioimaging [60]. Single QD studies offer ultrahigh sensitivity for single-molecule detection [61].

Plasmonic nanostructures, such as nanoparticles [62], nanorods [63], and nanoholes [64] have been investigated to enhance QD fluorescence. However, positioning single QDs onto plasmonic nanostructures remains challenging, which is crucial for achieving plasmon-enhanced fluorescence [65] [66][67]. Nanohole arrays in thin metal films present a promising solution for this purpose, as the electromagnetic hotspots form within each nanohole under resonant illumination. When combined with an inverted fluorescence microscope for fluorescence imaging with light coming from the glass side, only QDs within the nanoholes are detected, while those deposited on the metal surface are obscured by the opaque metal film.

4.2.1 Simulation of the plasmonic nanohole arrays

The plasmonic peaks of nanohole arrays, in terms of peak position and intensity, mainly depend on the optical properties of the metal film, structural parameters of nanoholes, incident light direction, and dielectric environment [68], [69]. Using COMSOL Multiphysics, we designed a nanohole array with a plasmonic peak near the fluorophore excitation wavelength. The simulation employed a linearly polarized incident plane wave as the background wave, utilizing one-fourth of a nanohole with perfect electric conductor (PEC) and perfect magnetic conductor (PMC) boundaries to represent an infinite nanohole array laterally in the plane. The PEC and PMC boundary sides were aligned perpendicularly and in parallel to the electric field polarization direction of the incident plane waves, respectively. Perfectly matched layers (PMLs) absorbed scattered waves both above and below the structure to prevent non-physical reflections, see Figure 4.3a. Two planes were set to monitor ports to detect the reflectance (R) and transmittance (T), one above and the other below the structure, with the input expressions (written in script for the simulation implementation) below:

$$I = intop1(n_{glass} * 0.5 * real(-ewfd.E_{bz} * conj(ewfd.H_{by}) + ewfd.E_{by} * conj(ewfd.H_{bz})))$$

$$T = intop2(ewfd.P_{oavx})/I$$

$$R = (I - intop1(ewfd.P_{oavx}))/I$$

$$A = intop3(ewfd.Q_h)/I$$

where, I is the intensity of incident wave, A is the absorption in the Al layer, *intop* the integration of an expression over a source like specific plane or domains, P_{oavx} the X-component (the wave propagation direction) of time-

averaged power flow, n_{glass} the refractive index of the glass substrate, and Q_h the energy loss in the Al film. The simulation ensured that $T + R + A = 1$.

In an aqueous environment, the thickness of the Al film (*t*), the diameter of the nanoholes (*D*), and the period of the nanohole array (*p*) were optimized to be 30 nm, 110 nm, and 300 nm, respectively, to have a transmittance maximum peak around the 515 nm excitation wavelength. The Al optical constants, measured using ellipsometry, were applied in the simulation. The simulated cross-sectional distribution of enhanced electric field in the central part of a nanohole is shown in Figure 4.3b. The electric field intensity is enhanced inhomogeneously in the nanohole volume with maxima at the edges. The transmittance maximum peak is also the plasmonic peak at which the plasmonic resonance occurs and the local electric field reaches its maximum [64]. For the optimization of these three structural parameters, the square of average electric field amplitude of the nanohole volume was used as the figure of merit at the 515 nm excitation light from the glass side. The effects of these three structural parameters on transmittance peak were investigated, as shown in Figure 4.3d–f. The transmittance peak position red shifts with *D* and *p*, but blue shifts with *t*.

To calibrate the simulation model, the transmittance spectrum of another array with a 270 nm period was measured in air with a spectrophotometer equipped with an integrating sphere, see the schematic in Figure 4.3c. After careful calibration of the transmittance measurement, the measured transmittance spectrum agreed well with the simulation results (see Paper I).

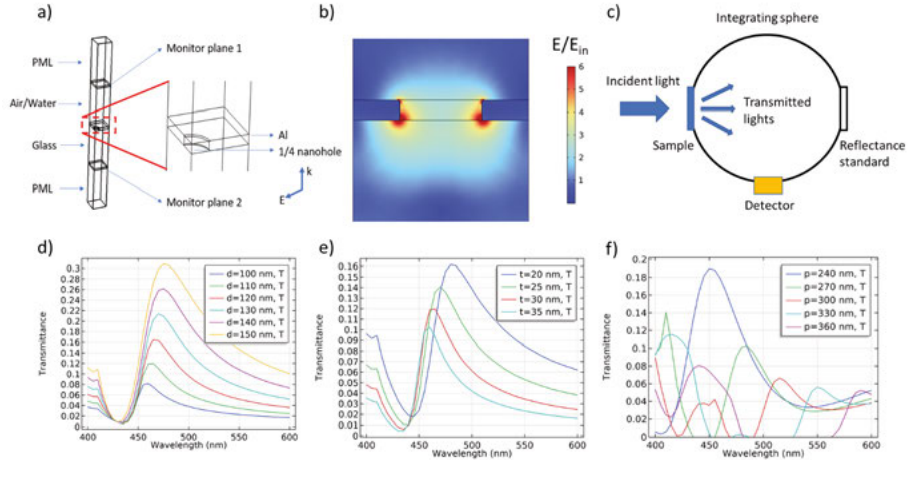

Figure 4.3 (a) Simulation model of the one-quarter nanohole to represent an array. (b) Simulated electric field distribution in the central cross-section of a nanohole. (c) Schematic spectrophotometer setup for the transmittance measurements. Simulated average enhanced electric field in the nanohole volume for nanohole arrays with different diameters (d), thicknesses (e) and periods (f). (b) is adapted from Paper I with permission of American Chemical Society. Copyright (2023) American Chemical Society.

Considering the fabricated nanoholes with unavoidably inhomogeneous diameters and shapes, their effects on the plasmonic peak were also investigated by means of simulation. The simulation results show that they have little effect on the plasmonic peak position, see Figure 4.4.

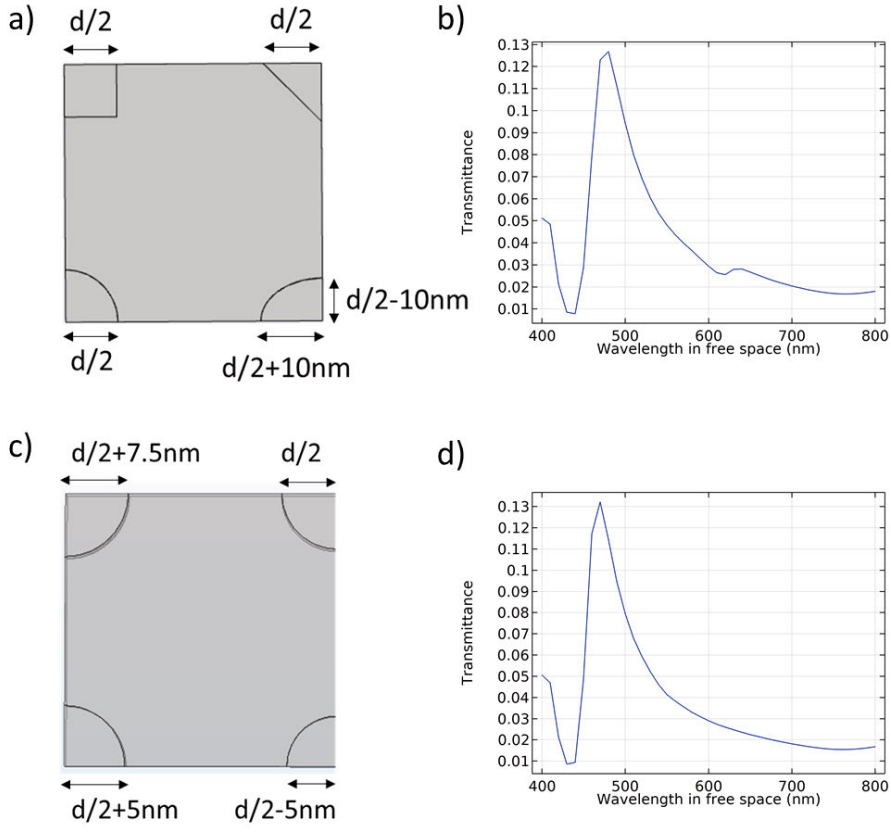

Figure 4.4 (a) A simulated unit cell (one quarter) of nanoholes with different shapes. (b) The simulated transmittance spectrum of the nanohole array based on (a). (c) A simulated unit cell (one quarter) of nanoholes with different diameters. (d) The simulated transmittance spectrum of the nanohole array based on (c).

4.2.2 Fabrication of nanohole arrays and QD immobilization

The nanohole arrays were fabricated using the same process flow described in Figure 4.1a. An optical image of a fabricated chip consisting of nanohole arrays with different periods and diameters is shown in Figure 4.5a, indicating that different periods have different colors due to plasmonic resonance effects. Although the SF_6 and O_2 gas mixture was used to remove residue Cl in the etching recipe, there was still some Cl left causing “mouse bites” or “worm holes” in the Al film, see Figure 4.5b. After immersing the chip into heated DI water instantly after ICP-RIE to totally remove residue Cl, these defects

were eliminated (Figure 4.5c). A commercial silicone well with a sticky bottom was mounted on top of the chip to load solutions.

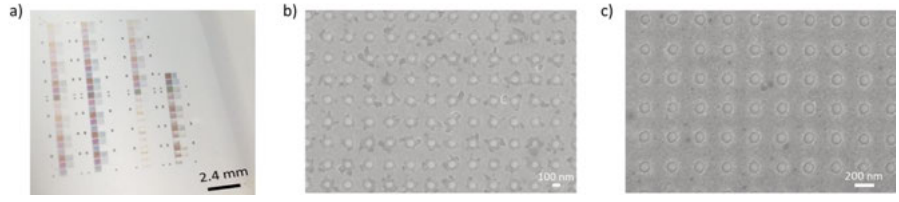

Figure 4.5 (a) An optical image of nanohole arrays with different periods and nanohole diameters. (b) A top-view SEM image of a fabricated nanohole array without rinsing in water after dry etching. (c) A top-view SEM image of a fabricated nanohole array with rinsing in water after dry etching.

To immobilize colloidal streptavidin-conjugated QDs (SA-QDs), the surface of nanoholes was first functionalized with poly(vinylphosphonic acid) (PVPA) and silane-PEG-biotin. PVPA was used to prevent non-specific adsorption, while silane-PEG-biotin would help capture the colloidal SA-QDs through the streptavidin-biotin bonding [70] (see Paper I). After incubation and washing, single SA-QDs were immobilized inside the nanoholes.

Other surface functionalization methods were also investigated including PLL-biotin only, PVPA only, and combinations of PVPA and PLL-biotin (Figure 4.6). Micron-sized Al grids were first created on a glass substrate using photolithography, magnetron sputtering, and lift-off. The colloidal SA-QDs were incubated and washed in different containers according to the functionalization method used. The chip was then flipped and mounted on another glass substrate with water in between. Positively charged PLL-biotin adsorbed on both Al and glass, assisting immobilization of SA-QDs on both surfaces. The SA-QDs could physically adsorbed on both bare Al and glass without any surface functionalization, but they were not immobilized. However, negatively charged PVPA significantly reduced nonspecific adsorption of SA-QDs on Al. PLL-biotin adsorbed on the PVPA-coated Al. The combination of PVPA and silane-PEG-biotin was found to be the most effective in passivating Al while immobilizing SA-QDs on glass, see the summary in Table 4.1.

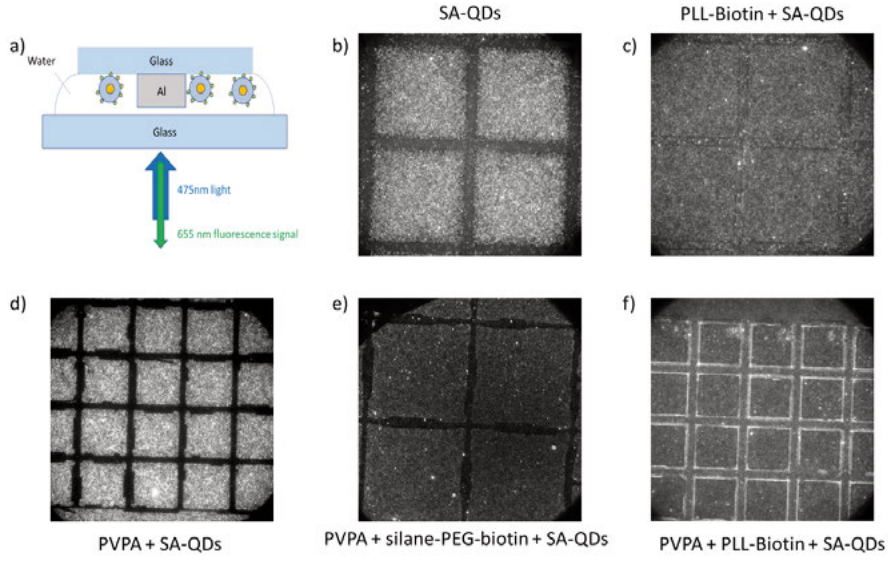

Figure 4.6 (a) Schematic of the fluorescence imaging setup for characterizing the surface functionalization on Al grids and glass for SA-QDs. (b-f) Fluorescence images of SA-QDs: without any surface functionalization (b), with PLL-biotin (c), with PVPA (d), with PVPA and silane-PEG-biotin (e), and with PVPA together with PLL-biotin (f). View sizes of (b–f) are all 133 µm × 133µm.

Table 4.1 Adhesion and immobilization results (Yes or No) of SA-QDs on a glass substrate with different surface functionalization methods.

	Bare	PLL-biotin	PVPA	**PVPA & Silane-PEG-biotin**	PVPA & PLL-biotin
Glass	Yes, No	Yes, Yes	Yes, No	**Yes, Yes**	Yes, Yes
Al	Yes, No	Yes, Yes	No, No	**No, No**	Yes, Yes

4.2.3 Fluorescence imaging and analysis of single QDs

The concentration and volume of the SA-QD solution were optimized to achieve a suitable density of immobilized SA-QDs both on the bare glass substrate and in nanoholes, as shown in the fluorescence images in Figure 4.7a–d. The average distance between SA-QDs was larger than the diffraction limit of the widefield fluorescence microscope. Correlation between SEM and fluorescence images in the same area confirmed that most detected fluorescent spots were single SA-QDs rather than clusters, as depicted in Figure 4.7e–f.

A commercial coverslip with etched grids into the glass as markers was used for the correlation, see Figure 4.7g. A 4 nm-thick Au/Pd alloy was deposited on top of the single QDs on the coverslip before SEM to eliminate the charging effect, a zoom-in SEM image is shown in Figure 4.7h.

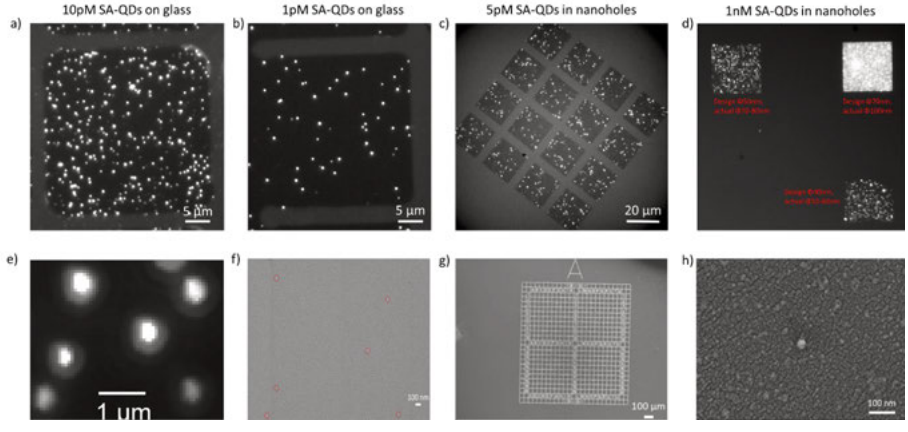

Figure 4.7 (a-b) Fluorescence images of single SA-QDs immobilized on a glass substrate with concentration of 10 pM (a) and 1 pM (b) but with the same volume. (c) A fluorescence image of SA-QDs (5 pM concentration) immobilized in the nanohole arrays. (d) A fluorescence image of SA-QDs (1nM concentration) immobilized in nanohole arrays with different diameters. (e) A zoom-in fluorescence image of single QDs on a glass substrate. (f) An SEM image of single QDs in the same area as in (e). (g) A commercial glass substrate with etched grids for correlating between fluorescence images and SEM images in (e) and (f). (h) A zoom-in SEM image of a single QD on a glass substrate coated by 4 nm thick Au/Pd.

The blinking characteristics of single SA-QDs were recorded during fluorescence imaging. During analysis, the pixels of single SA-QDs were selected by setting a background intensity threshold, see Figure 4.8a. The time sequences of the mean intensity of the selected pixels were then extracted from the recorded video, as illustrated in Figure 4.8b-c. The difference between the average values of ON-states and OFF-states was used as the fluorescence intensity of a single QD. The photobleaching effect was also observed: with a high illumination light intensity and a long illumination time, the intensity of a QD decreased with time, as shown in Figure 4.8c.

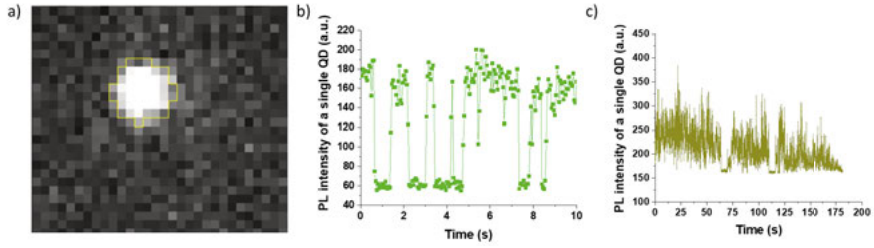

Figure 4.8 (a) A fluorescence image of a single SA-QD immobilized on a glass substrate. The pixels within the yellow frame were selected by an intensity threshold value for analyses. (b) The time series blinking characteristics of a single SA-QD with low illumination light intensity for 10 s. (c) The time series blinking characteristics of a single SA-QD with high illumination light intensity for 60 s. Both (b) and (c) had a frame rate of 0.05 s/frame.

To investigate the plasmon-enhanced fluorescence, a fluorescence microscope with a monochromatic 515 nm diode laser source in bright-field imaging mode was used, as shown in Figure 4.9a. A typical fluorescence image of QDs in nanoholes is presented in Figure 4.9b. The inhomogeneous intensity distribution of focused laser spot was calibrated, see Figure 4.9c. Statistical results of the fluorescence intensities of single QDs showed that the PL peak intensity of single QDs on the bare glass substrate was around 1300, while those in nanohole arrays with p = 300 nm peaked around 6300, indicating an overall 5-fold enhancement (*i.e.*, 6300/1300), as shown in Figure 4.9d–e. The measured fluorescence intensities of single QDs in nanohole arrays with different periods correlated well with the trend of simulation results using the square of electric field enhancement in the nanohole volume as the figure of merit, see Figure 4.9f.

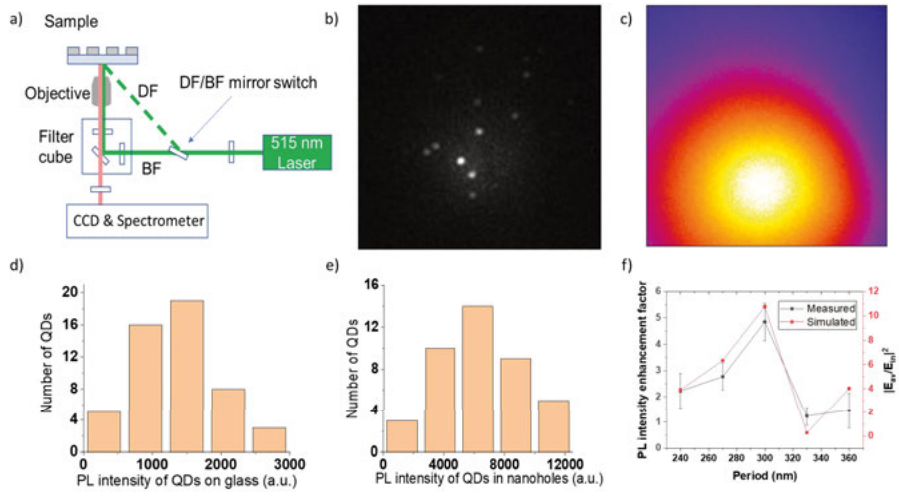

Figure 4.9 (a) Schematic of the fluorescence microscope setup. (b) A fluorescence image of single QDs in nanoholes with bright-field imaging mode. (c) The intensity distribution of the laser spot focused on the substrate. (d) The analyzed pixels of a single QD within the yellow line according to a threshold value. (d–f) are adapted with permission from Paper I. Copyright (2023) American Chemical Society.

4.3 Plasmon-enhanced fluorescence analysis of single extracellular vesicles (EVs) in Al nanoholes

Extracellular vesicles (EVs) are cell-derived nanovesicles encapsulated by a lipid bilayer membrane. They contain a variety of cellular components including proteins, DNA, RNA, lipids and consequently play important roles in numerous pathological and physiological processes. Their ability to transfer biologically active constituents to a recipient cell makes them an important factor in intercellular communication [71]. Their high heterogeneity in molecular compositions presents a significant challenge for the identification of cellular origin and/or biological functions [72]. Studies of single EVs are thus crucial for identifying and detecting sEVs with disease-specific signatures [73]. Fluorescence-based methods have been widely used to study membrane proteins, such as CD9, CD63, and CD81 on single small EVs (sEVs) [74]. However, the highly heterogeneous expression levels of these tetraspanins make profiling difficult, as proteins with low expression levels are often undetected during fluorescence analysis. In this study, sEVs derived from the human embryonic kidney (HEK293) cell line were used, and their CD9 expression was analyzed using fluorescently-tagged anti-CD9 antibodies.

The plasmonic nanohole arrays in a thin metal film can enhance the fluorescence intensity of molecular fluorophores commonly used in immunostaining for biosensing and bioimaging, thereby increasing the detection sensitivity

of fluorophore-tagged biotargets such as proteins and EVs [75], [76]. However, for single sEV studies using the reflection mode of the plasmonic nanohole array, the mirror effect of the metal film can strongly influence the fluorescence intensity, complicating the analysis of plasmonic effects in the nanohole volume [77]. By combining nanohole arrays in a thin Al film with an epi-fluorescence microscope with light incident from the glass side, only the single sEVs immobilized inside the nanoholes would be detectable, as illustrated in Figure 4.10.

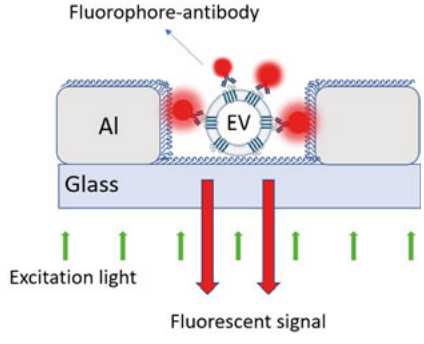

Figure 4.10 Schematic of a single sEV immobilized inside a functionalized nanohole in a thin Al film on a glass substrate. Excitation light illuminates from the glass side and the plasmon-enhanced fluorescent signal is detected on the same side.

4.3.1 Simulation and fabrication of Al nanohole arrays for capturing single sEVs

The mean and mode sizes of the bio-engineered sEVs with mNG fluorescent protein tagged to CD63 (mNG-sEVs) were 129 ± 1 nm and 117 ± 3 nm, respectively. The mean and mode sizes of the wild-type sEVs (wt-sEVs) were 171 ± 5 nm and 148 ± 4 nm, respectively, see the NTA results in Paper II and the AFM measurement of single sEVs on a PLL-glass substrate in Figure 4.11a–b. To capture single sEVs while preventing multiple sEVs from entering one single nanohole, the nanohole diameter was designed to be 200 nm. The Al film thickness was fixed at 40 nm, and three periods were set to 305 nm, 340 nm, and 430 nm to achieve a transmittance peak, *i.e.* a peak of electric field enhancement in the nanohole volume, around 515 nm for the excitation wavelength, as shown in Figure 4.12a–b. The simulation model settings were the same as those for the data in Figure 4.3a.

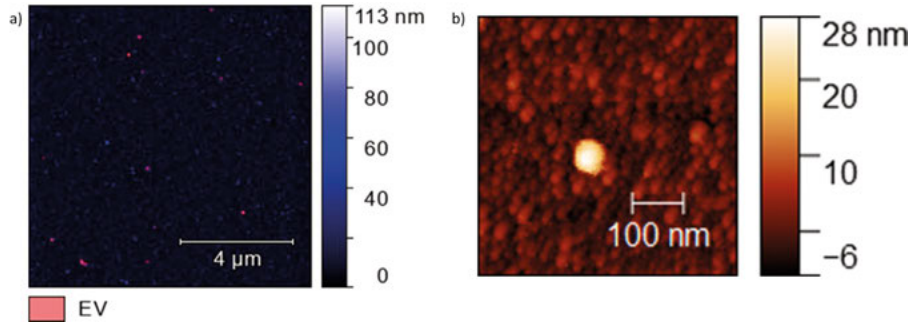

Figure 4.11 (a) An AFM image of single sEVs on a PLL-functionalized bare glass substrate using the low-resolution scanning mode. Particles with height above 50 nm are labeled with a red mask. (b) An AFM image of a single sEV on a PLL-functionalized bare glass substrate.

The nanohole arrays were fabricated using the same process flow described in Figure 4.1a, with the fabricated nanoholes shown in Figure 4.12c. A silicone well was mounted on top of the chip, again on the front side, for loading samples and solutions. The surface of the nanohole arrays was functionalized with positively charged PLL in order to capture the negatively charged sEVs. The mNG-sEVs were used to optimize surface functionalization protocol, solution concentration and volume, and immunostaining protocol with R-PE-tagged anti-CD9 antibodies. Fluorescence imaging and AFM measurement confirmed the successful capture of wt-sEVs in the nanoholes (Figure 4.12d–f). The fluorescence microscope setup was the same as in Figure 4.9a. The wt-sEVs, with a larger proportion of CD9-positive sEVs than the mNG-sEVs, were used to investigate the plasmonic effects of the nanohole arrays, as shown in Figure 4.13.

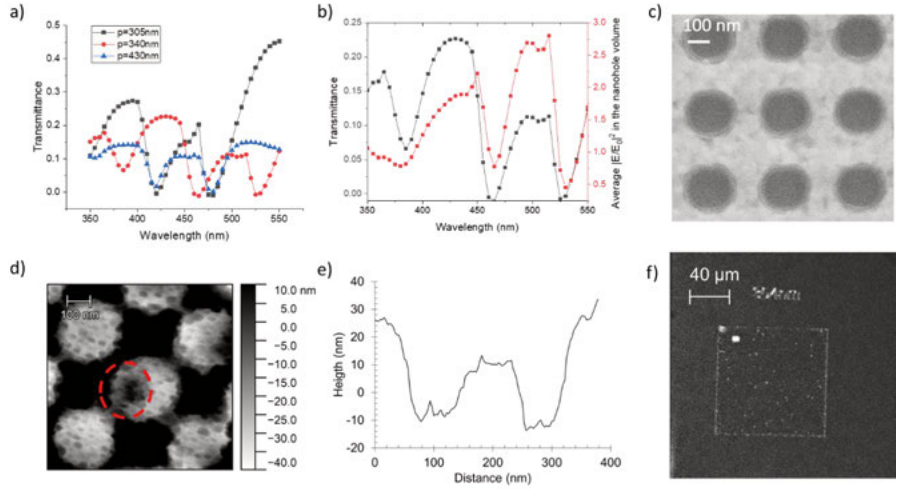

Figure 4.12 (a) Simulated transmittance spectra of nanohole arrays with periods of 305 nm, 340 nm, and 430 nm. (b) Simulated transmittance spectrum and average $|E/E_0|^2$ in the nanohole volume of the nanohole array with a period 340 nm. (c) A top-view SEM image of the fabricated nanohole array. (d) An AFM image of a single wt-EV inside a nanohole. (e) Height profile across the nanohole in (d). (f) A fluorescence image of R-PE tagged wt-EVs inside a nanohole array with dark-field imaging mode.

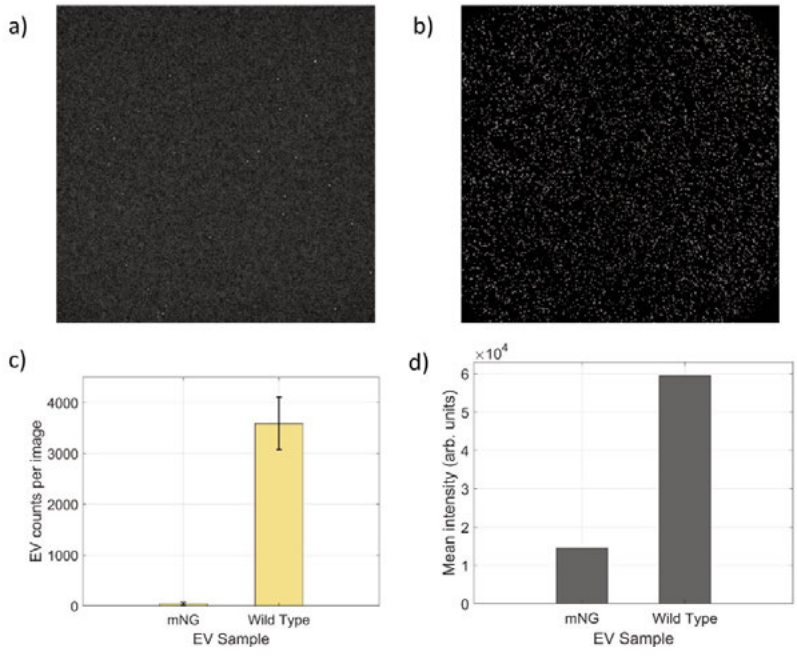

Figure 4.13 Representative fluorescence images of R-PE signals from anti-CD9-R-PE stained mNG-EVs (a) and wt-EVs (b), with a view size of 133 μm × 133 μm. (c) Average number of detected EVs per image for both samples. Twenty images were taken for both samples to obtain the average. (d) Mean fluorescence intensities of both samples.

4.3.2 Fluorescence imaging and analysis of single wt-sEVs in Al nanohole arrays

Wt-sEVs stained with R-phycoerythrin conjugated anti-CD9 antibody were detected inside the nanoholes using an epi-fluorescence microscope, as shown in Figure 4.14a–d. For quantitative fluorescence intensity analysis, a control substrate after the Al etching on the same chip was used as a reference. To calibrate the inhomogeneous intensity of the laser spot, the ratio of fluorescence signal to local laser spot intensity (I_{signal}/I_{laser}) was calculated in pixels for an accurate quantification of fluorescence enhancement due to plasmonic effects. The histograms of fluorescence intensities of sEVs and the density of detected bright spots in different arrays are shown in in Figure 4.14e–f. Both the overall fluorescence intensity and the number of detected bright spots were larger in all three nanohole arrays compared to the reference substrate. The experimental values for different nanohole periods qualitatively agree with the trend predicted by the simulation. The overall 1.3-fold plasmon-enhanced fluorescence contributed to a more than 12-fold increase in detected sEV counts, revealing a large number of weekly fluorescent sEVs, *i.e.* those with generally lowly expressed protein targets on the surface. This work, therefore, provides a basis for highly sensitive and unbiased single-sEV fluorescent detection and analysis.

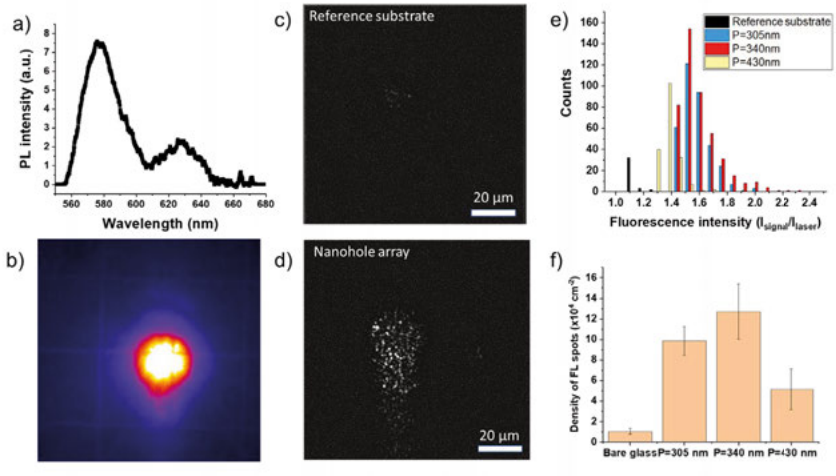

Figure 4.14 (a) Measured fluorescence emission spectrum of the R-PE fluorophore. (b) Intensity distribution of the focused 515 nm laser spot in bright-field mode, view size 100 µm × 100 µm. (c) A fluorescence image of R-PE tagged wt-sEVs on a reference substrate (bare glass) as control. (d) A fluorescence image of R-PE tagged wt-sEVs inside a nanohole array on the same chip as (c). (e) Histograms showing the fluorescence intensity distribution of wt-sEVs on the reference substrate and in nanohole arrays of p=305 nm, 340 nm, and 430 nm, all with t=30 nm and D=200 nm. (f) Histograms of the density of detected FL spots in these three different nanohole arrays and on the reference substrate.

4.4 Plasmon-enhanced photoluminescence of single UCNPs with gold nanorod dimers

To enhance the photoluminescence intensity of UCNPs, various plasmonic nanostructures, besides engineering the elemental composition and structure of UCNPs [78], [79], have been investigated; the nanostructures include colloidal gold nanoparticles [80], colloidal gold nanorods [81], Al nanocylinder arrays [82], nanoholes or nanocavities in a gold film [83], [84], silver nanogratings [85], silver nanocubes and gold film [86], and two-dimensional photonic crystal structures [87]. However, for single UCNP-based studies, it is critical but challenging to precisely control the spatial positioning of single UCNPs relative to the plasmonic nanostructures. While template-assisted self-assembly and AFM methods have been employed to achieve such a control [80], [81], [88], these techniques suffer from low loading efficiency and require specialized equipment.

In this chapter, we designed gold nanorod dimers (GNRDs) by carrying out systematic simulations to achieve a plasmonic peak that overlaps the excitation wavelength of UCNPs. The GNRDs were fabricated via EBL, followed by evaporation and lift-off processes. Subsequently, electron-beam induced deposition (EBID) was utilized to create carbon nanodomains (CNDs) in the gaps of GNRDs, facilitating the selective capture of single UCNPs via streptavidin-biotin bonding. The local electromagnetic field at the GNRD gaps was significantly enhanced due to LSPR, contributing to a substantial increase in upconverted photoluminescence.

4.4.1 Simulation and fabrication of the GNRDs

The GNRDs on a SiO_2 substrate in an aqueous environment were designed and optimized with the assistance of COMSOL simulations to achieve a plasmonic peak overlapping with the excitation wavelength for UCNPs. The simulation schematics are illustrated in Figure 4.15a–c, where the surroundings of the model are perfectly matched layers (PMLs). Light illuminates from the top along the -Z direction. The rounded ends of the GNRD in the model are proximate real structures. The scattering field from a bare SiO_2 substrate (without the GNRD) serves as the background field for simulations involving the GNRD on SiO_2. The optimized GNRD dimensions are 155 nm in length, 50 nm in width, and 50 nm in thickness, with a 50 nm gap in the middle. The electric field enhancement is primarily concentrated at the GNRD gap, achieving approximately a 10-fold increase, as shown in Figure 4.15d–e. The absorption cross section peaks at the LSPR, as depicted in Figure 4.15f.

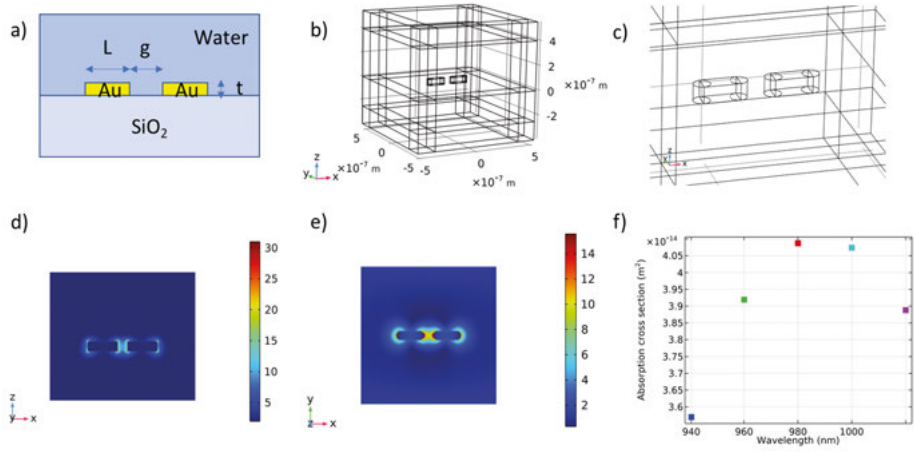

Figure 4.15 (a) A cross-section schematic of a GNRD structure on a SiO_2 substrate in water environment, with the structural parameters indicated as L (length), g (gap), and t (thickness). (b) The model built in the simulation has PMLs surrounded to absorb scattered waves. (c) Zoom-in of the model in (b). The GNRD are modeled with rounded ends to better approximate the fabricated structures. (d) The distribution of electric field enhancement from cross-sectional view. (e) The distribution of electric field enhancement from top-view. (f) Simulated plasmonic spectrum of the GNRD in the wavelength range of 940 nm to 1020 nm, using the absorption cross-section as the figure-of-merit.

To explore the influence of structural parameters including nanorod length and width, gap size, light polarization, and the dielectric environment on the plasmonic peak of the GNRD, we used the absorption cross section as an indicator, as shown in Figure 4.16. Increasing the GNRD length results in a redshift of the plasmonic peak, while the width of GNRD also significantly affects the peak, as illustrated in Figure 4.16a–c. An increase in the gap size from 50 nm to 150 nm induces a blueshift in the plasmonic peak, attributed to the decreased Coulomb force between opposite charges in the two GNRs, which leads to a higher electron oscillation frequency for LSPR and thus a shorter wavelength (Figure 4.16d). The plasmonic peak is also highly sensitive to the dielectric environment, with an increase in the refractive index from 1 to 1.5 causing a redshift, as depicted in Figure 4.16e. Additionally, the electromagnetic field enhancement is polarization-dependent, occurring primarily along the X-axis, not in the Y-axis (Figure 4.16f).

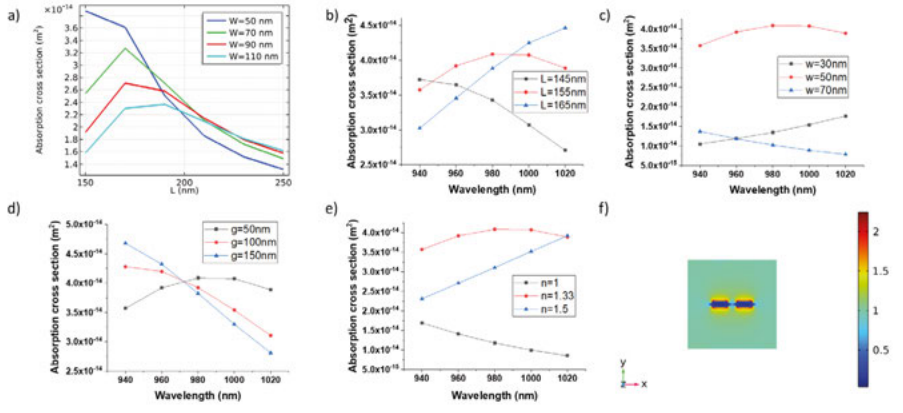

Figure 4.16 A comprehensive analysis of the simulated effects of various parameters on the plasmonic peak and absorption cross-section of the GNRD. (a)–(f) demonstrate how the dimensions, gap distance, dielectric environment, and polarization of the GNRD affect the plasmonic behavior.

The fabrication of the designed GNRDs on a SiO_2-Si substrate involves lithography, evaporation, and lift-off steps, with the process flow schematics shown in Figure 4.17a. Top-view SEM images of the fabricated GNRDs are presented in Figure 4.17b–c. Despite inevitable fabrication deviations, the lithography-based processes allow for precise control of the GNRD positions and structural parameters, facilitating easy integration with other nanoparticles or nanodevices.

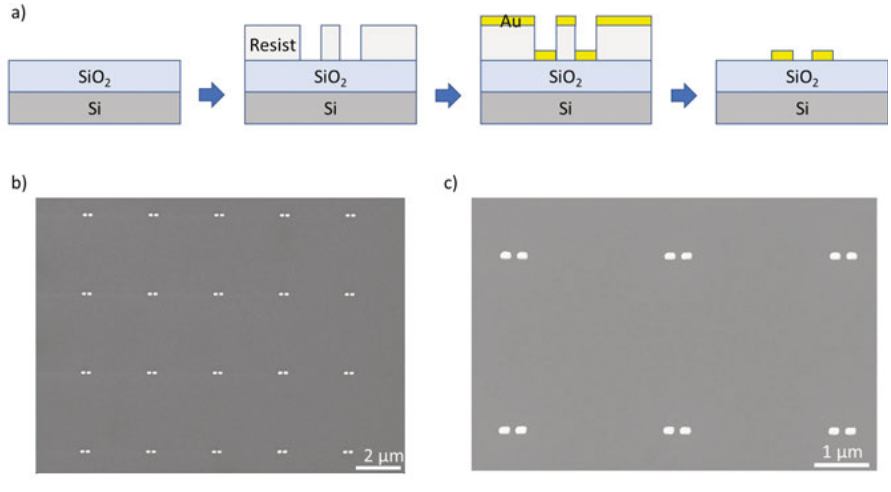

Figure 4.17 (a) Schematics of the fabrication process. (b) A top-view SEM image of the fabricated GNRDs. (c) A zoom-in SEM image of GNRDs in (b).

4.4.2 Site-specific capturing of single UCNPs

To demonstrate that EBID can be used for site-specific capture of single UCNPs, a bare Si substrate covered by a 150 nm-thick SiO_2 layer was first functionalized with mPEG-silane. Carbon nanodomains (CNDs) were then created within the mPEG-silane layer using EBID. The mPEG-silane layer prevents non-specific protein adsorption, whereas the CNDs selectively adsorb proteins such as streptavidin [89], [90], thereby enabling the capture of single SA-UCNPs or biotin-UCNPs on CNDs, as illustrated in Figure 4.18a–d. The CNDs were of less than 200 nm in diameter, primarily determined by the electron beam dose during EBID. Larger CNDs increase the occupancy ratio of UCNPs but at the cost of reduced positional accuracy and probability of having a single UCNP. Statistically, the overall UCNP occupancy on CNDs reached 25%, with single UCNP occupancy at 12% for an electron beam dose of 240 C/m^2 (corresponding to a CND diameter of 200 nm, as shown in Paper IV).

Subsequently, CNDs were fabricated at the gaps of GNRDs using the same set of alignment marks for EBL, as shown in Figure 4.18e. Following the incubation of colloidal UCNPs, approximately 24% of the GNRDs had UCNPs located at the gap, with half containing a single UCNP and the other half containing multiple UCNPs. A representative SEM image of a single UCNP captured at the gap of a GNRD is shown in Figure 4.18f.

The EBID technique was further investigated for different substrates, surface functionalization schemes (with different molecules), and fluorophores. For example, ITO-coated glass substrates, which are compatible with fluorescence microscopy for bioimaging, can be functionalized with PVPA [90], followed by EBID to create CNDs. This functionalization scheme allows for selective protein adsorption, as evidenced by the successful capture of SA-Cy5 and SA-QDs on the CNDs (Figure 4.19a–c). The method is also applicable to SiO_2-Si substrates coated with a 30 nm-thick Al_2O_3 layer, as shown in Figure 4.19d–e. Additionally, nanoholes can be created in the Al_2O_3 layer, enabling selective capturing of fluorophores on the bottom SiO_2 surface inside the nanoholes after appropriate surface functionalization with PVPA and silane-PEG-biotin on Al_2O_3 and SiO_2, respectively (Figure 4.19f–g). For SiO_2-Si substrates, the excitation light for fluorescence imaging must be incident from the top side, whereas for glass substrates it can be incident from either the top or the bottom side. A summary of these investigations is presented in Table 4.2.

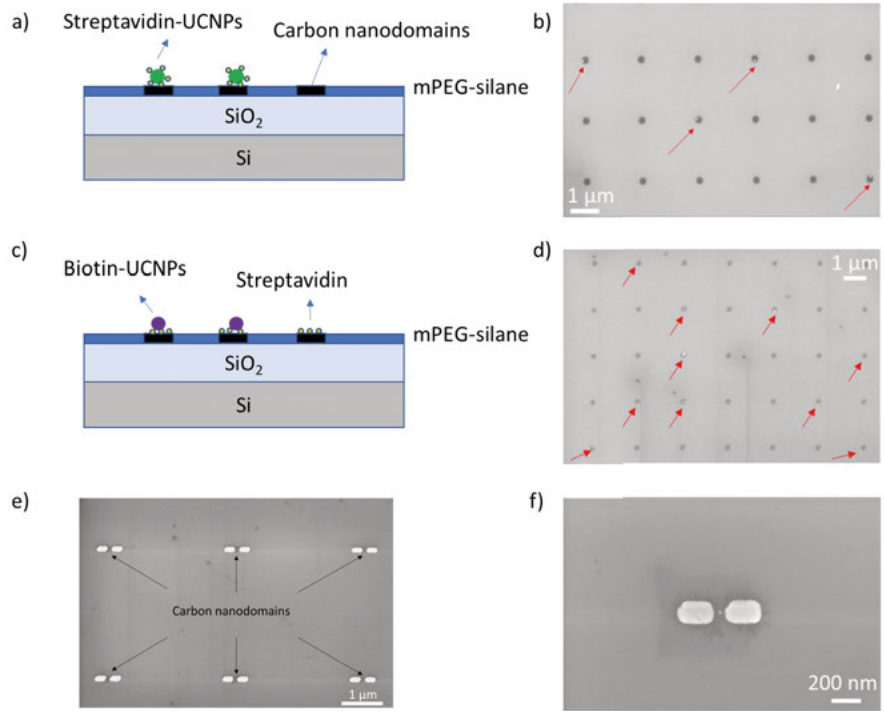

Figure 4.18 (a) Schematic of SA-UCNPs selectively captured on CNDs in a mPEG-silane layer on a SiO_2-Si substrate. (b) A top-view SEM image of SA-UCNPs on CNDs. (c) Schematic of biotin-UCNPs selectively captured on SA-functionalized CNDs in the mPEG-silane layer on a SiO_2-Si substrate. (d) A top-view SEM image of biotin-UCNPs on SA-functionalized CNDs. (e) A top-view SEM image of CNDs at the gaps of GNRDs. (f) A representative SEM image of a single SA-UCNP captured on a CND at the gap of a GNRD.

Table 4.2 Summary of EBID tests on different substrates with various surface functionalization chemicals and adsorbed molecules.

	mPEG-silane	PVPA
SiO_2-Si	SA-UCNPs, SA-biotin-UCNPs	–
Al_2O_3-SiO_2-Si	–	SA-Cy5, Neutravidin ([89])
ITO-glass	Avidins ([88])	SA-Cy5, SA-QDs

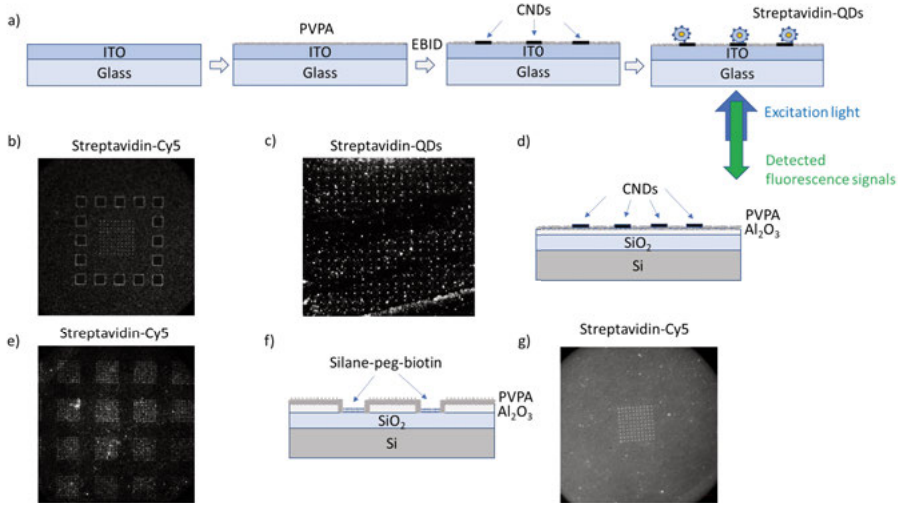

Figure 4.19 (a) Schematics of EBID process on a PVPA-functionalized ITO-glass substrate. (b) A fluorescence image of an array of selectively captured SA-Cy5 on a substrate of (a). (c) A fluorescence image of an array of selectively captured SA-QDs on a substrate of (a). (d) Schematic of the CNDS in a PVPA layer on SiO_2-Si substrate with an Al_2O_3 layer. (e) A fluorescence image of arrays of SA-Cy5 on a substrate of (d). (f) Schematic of selective surface functionalization on nanoholes in an Al_2O_3 layer on a SiO_2-Si substrate. (g) A fluorescence image of selectively captured SA-Cy5 on a substrate of (f).

4.4.3 Fluorescence imaging and analysis of single UCNPs

Photoluminescence imaging of single UCNPs typically requires a high excitation laser power density due to the low quantum yield of UCNPs [34]. However, this high power-density can also generate two-photon induced fluorescence from the GNRDs [91]. Here, a multiphoton scanning microscope with a pulsed laser was used for imaging UCNPs alongside GNRDs with a relatively low power density to avoid the undesired effects of two-photon fluorescence. At high power densities, fluorescence signals from both GNRDs and UCNPs were detected, even within a narrow detection range covering the emission peaks of UCNPs. This overlap occurred because the two-photon induced fluorescence from gold has a broad spectrum that includes the visible emission peaks of UCNPs [91]. This issue can be mitigated by carefully lowering the power density, coating a thin layer of Al_2O_3 on the GNRDs, or detecting the UV-blue emission peaks of UCNPs instead, *i.e.*, outside the fluorescence spectrum from gold. When the power density was reduced, UCNPs were still excited, but the signals from GNRDs disappeared, as shown in Figure 4.20a–b. Note that the UCNPs were not site specifically immobilized at the gap of GNRDs here. After depositing a 30 nm thick Al_2O_3 layer on the GNRDs using ALD, the fluorescence signals from the GNRDs were effectively suppressed at the same power density, as shown in Figure 4.20c–d.

However, during imaging, some trailing artifacts, or "tails" from the UCNPs were observed when the scanning speed was high. This streaking effect occurred due to the long lifetime of the UCNPs [92].

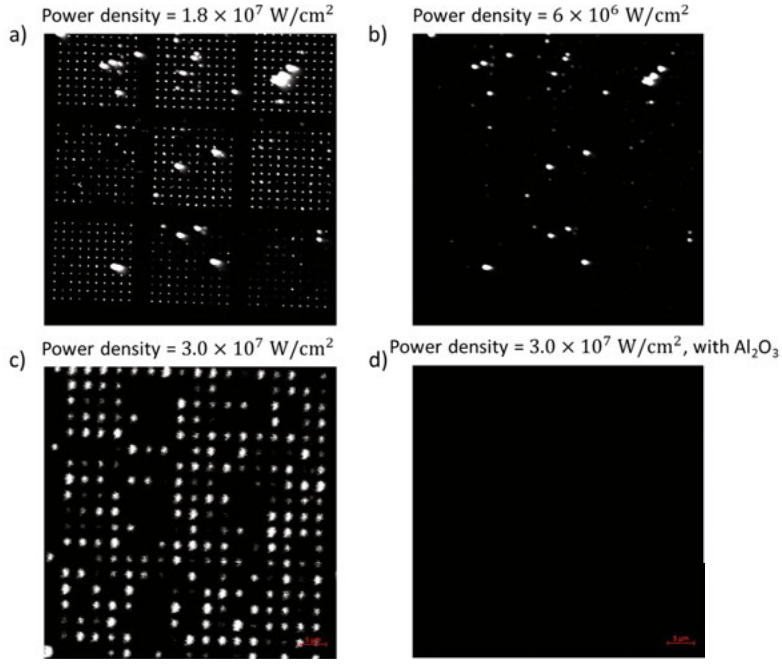

Figure 4.20 Multiphoton induced fluorescence from GNRDs during the imaging UCNPs. (a) A PL image of UCNPs on GNRD arrays at a power density of 1.8×10^7 W/cm^2. (b) A PL image of the same area as in (a), but at a reduced power density of 6.0×10^6 W/cm^2. (c) A PL image of a GNRD array without UCNPs at a power density of 3.0×10^7 W/cm^2. (d) A PL image of the same area as in (c), following the deposition of a 30 nm Al_2O_3 layer, with the same power density.

Optimized PL imaging showed that the PL intensities of single UCNPs in the gaps of GNRDs were enhanced by about 3-fold at $4 \times 10^6\,\mathrm{W/cm^2}$ excitation power density, see Figure 4.21. The power density value was already in the saturation regime of the UCNPs. A lower power density and a better alignment between the laser polarization direction with the longitude axis of GNRDs shall give a higher PL enhancement.

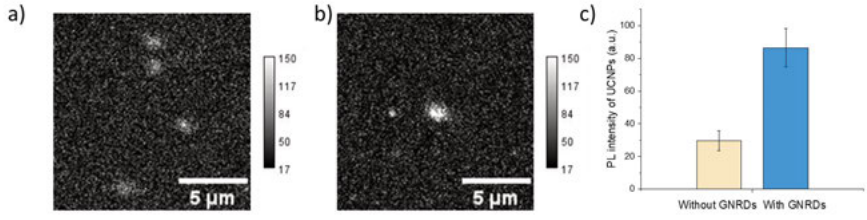

Figure 4.21 (a-b) PL images of single UCNPs on CNDs only without GNRDs (a) and with GNRDs (b). (c) Statistics of the PL intensities of single UCNPs without and with GNRDs.

5 Summary and outlook

The ultimate goal of this thesis is to achieve SMD in electrolyte with a novel optoelectronic device as a portable and cost-effective sensing platform. Phototransistors on chips are investigated for this purpose. The advantages of fluorescence-based methods and FETs are combined. Phototransistors are employed as the photodetectors to detect fluorescence signals from UCNPs without any optical filters. Specific molecular sensing is achieved via UCNP-based FRET. On the other hand, to improve SNR towards SMD, plasmonic nanostructures are employed to enhance fluorescence intensities of single fluorophores.

For the phototransistor-based molecular sensing platform, the main achievements include:

- Design and fabrication of α-IGZO: H TFTs with sub-micron distances between source and drain electrodes on silicon chips.
- Immobilization of SA-UCNPs on top between source and drain electrodes using surface functionalization.
- Mounting the chip onto a chip-holder on a PCB. Integration of electronic measurement system with a fluorescence microscope.
- Demonstration of FRET detection on the chip after adding biotin-AuNPs onto the chip. Order of magnitude estimation gives that each SA-UCNP generates a photocurrent-to-dark current ratio of 10^3 and each biotin-AuNP causes at least one order of magnitude decrease of the photocurrent.

For the plasmon-enhanced fluorescence studies, the main achievements are:

- Design of the structural parameters of Al nanohole arrays and GNRDs using numerical simulation to have a plasmonic peak at the excitation wavelength.
- Fabrication of simulation-guided Al nanohole arrays on a glass substrate and GNRDs on a silicon substrate with good control of their dimensions.
- Optimization of surface functionalization to immobilize single QDs and single EVs inside Al nanoholes, to selectively capture single UCNPs in the gaps of GNRDs using EBID.

- Using different fluorescence microscopes to image single QDs, single EVs, and single UCNPs. Plasmon-enhanced fluorescence intensities of these fluorophores are quantitatively analysed. Statistically, an overall 5-fold fluorescence intensity enhancement for single QDs, an overall 1.3-fold fluorescence intensity enhancement and 12-fold enhanced detected density for the molecular dyes on single EVs, and a 3-fold PL intensity enhancement for single UCNPs are achieved.

- The concept of integrating UCNPs and FRET with phototransistors as a novel platform for sensitive and specific molecular sensing is proved in the thesis. It can be applied to detect various molecules and biomarkers due to the power of FRET and versatile surface modifications on UCNPs. Moreover, the chip can be integrated with electronics, only a CW diode laser is needed in terms of optics. It is promising develop it into a portable and cost-effective biosensor.

- To achieve SMD, other photodetectors with more sensitive materials, such as perovskite, may be utilized to improve sensitivity. Besides, single UCNPs must be controlled and placed onto the phototransistors. Moreover, plasmonic nanostructures, such as GNRDs and nanoholes, can be further integrated onto the phototransistor for enhancing PL intensities of single UCNPs and the FRET efficiency.

6 Sammanfattning på Svenska

Det slutliga målet med denna avhandling är att uppnå SMD i elektrolyt med en ny optoelektronisk enhet som en portabel och kostnadseffektiv avkänningsplattform. Fototransistorer på chips undersöks för detta ändamål. Fördelarna med fluorescensbaserade metoder och FET kombineras. Fototransistorer används som fotodetektorer för att detektera fluorescenssignaler från UCNP utan några optiska filter. Specifik molekylär avkänning uppnås via UCNP-baserad FRET. Å andra sidan, för att förbättra SNR mot SMD, används plasmoniska nanostrukturer för att förbättra fluorescensintensiteten hos enstaka fluoroforer.

För den fototransistorbaserade molekylära avkänningsplattformen inkluderar de viktigaste resultaten:

• Design och tillverkning av a-IGZO: H TFT:er med submikronavstånd mellan source- och drainelektroder på kiselchips.
• Immobilisering av SA-UCNPs ovanpå käll- och dräneringselektroder med hjälp av ytfunktionalisering.
• Montering av chipet på en chip-hållare på ett PCB. Integrering av elektroniskt mätsystem med ett fluorescensmikroskop.
• Demonstration av FRET-detektion på chipet efter tillsats av biotin-AuNP på chipet. Storleksuppskattning ger att varje SA-UCNP genererar ett förhållande mellan fotoström och mörk ström på 1000 och varje biotin-AuNP orsakar minst en storleksordningsminskning av fotoströmmen.

För de plasmonförstärkta fluorescensstudierna är de viktigaste resultaten:

• Design av de strukturella parametrarna för Al nanohole arrays och GNRDs med numerisk simulering för att ha en plasmonisk topp vid excitationsvåglängden.

• Tillverkning av simuleringsstyrda Al nanohole arrays på ett glassubstrat och GNRDs på ett kiselsubstrat med god kontroll över deras dimensioner.

• Optimering av ytfunktionalisering för att immobilisera enstaka QD:er och enstaka EV:er inuti Al-nanohål, för att selektivt fånga enstaka UCNP:er i luckorna i GNRD:er med hjälp av EBID.

• Använda olika fluorescensmikroskop för att avbilda enstaka QD:er, enkla EV:er och enstaka UCNP:er. Plasmonförstärkta fluorescensintensiteter för dessa fluoroforer analyseras kvantitativt. Statistiskt sett uppnås en övergripande 5-faldig förbättring av fluorescensintensiteten för enstaka QDs, en

övergripande 1.3-faldig förbättring av fluorescensintensiteten och 12-faldig förbättrad detekterad densitet för de molekylära färgämnena på enstaka EVs och en 3-faldig PL-intensitetsförbättring för enstaka UCNP:er.

• Konceptet att integrera UCNP och FRET med fototransistorer som en ny plattform för känslig och specifik molekylär avkänning bevisas i avhandlingen. Det kan användas för att detektera olika molekyler och biomarkörer på grund av kraften i FRET och mångsidiga ytmodifieringar på UCNP. Dessutom kan chippet integreras med elektronik, endast en CW-diodlaser behövs vad gäller optik. Det är lovande att utveckla den till en bärbar och kostnadseffektiv biosensor.

• För att uppnå SMD, andra fotodetektorer med känsligare material, såsom perovskit, användas för att förbättra känsligheten. Dessutom måste enstaka UCNP:er kontrolleras och placeras på fototransistorerna. Dessutom kan plasmoniska nanostrukturer, såsom GNRD:er och nanohål, integreras ytterligare på fototransistorn för att förbättra PL-intensiteten hos enstaka UCNP:er och FRET-effektiviteten.

7 Acknowledgement

My PhD journey over the past five years has resembled the night sky—marked by a few bright, shining moments set against a backdrop of darkness, filled with frustrations and struggles. It would have been impossible to complete this challenging journey on my own. I would like to express my deepest gratitude to all those who have supported and helped me along the way.

First and foremost, I am profoundly grateful to my main supervisor, Prof. Shi-Li Zhang. Thank you for giving me this opportunity to embark on this journey, and for your guidance and support throughout these five years. I have learned so much from your deep and professional research knowledge, your research methodologies, and your insightful thinking, all shared during our weekly talks and discussions. I greatly admire your passion, energy, and diligence in research. Thank you for giving me the freedom and support to explore my own research interests while working towards the final goal of this project.

I am also deeply thankful to my co-supervisor, Assoc. Prof. Apurba Dev. Your detailed guidance and assistance in my research have been invaluable. It has always been a pleasure to discuss with you, as you have a remarkable ability to explain complex things in a straightforward and clear manner. The barbecues and group-dinners we shared are cherished memories for me.

Many thanks to group members for their kind help in the lab and for the valuable discussions during our weekly group meetings. I would like to acknowledge Dr. Ngan Pham, Dr. Yao Yao, Dr. Siddharth Sourabh Sahu, Moein Talebian Gevari, Fredrik Stridfeldt, Dr. Mohammad Hadi Khaksaran, Dr. Shiyu Li, Assis. Prof. Chenyu Wen, Dr. Won-Yong Lee, Dr. Sara Cavallaro, Dr. Federico Pevere, and Prattakorn Metem. I also appreciate the assistance of other colleagues from the solid-state electronics (FTE) division, including Dr. Shuangshuang Zeng, Dr. Xingxing Xu, Dr. Qitao Hu, Dr. Libo Chen, Assoc. Prof. Zhibin Zhang, Dr. Yingtao Yu, Dr. Yuan Zhu, Zheqiang Xu, Funing Liu, Assoc. Prof. Ted Johansson, Assoc. Prof. Tomas Nyberg, and Assoc. Prof. Tomas Kubart. Special thanks to Dr. Laurent Barbe and Dr. Federico Cantoni from the Microsystem Technology division for their help with microfluidics tests and training on various tools. I am also grateful to our HR, Linn Eriksson, and financial officers, Ida Näslund and Maria Brandt, for their help and support. A special thanks to Daniel Fernandes for the interesting daily conversations in the office.

I would also like to thank all the staff of the Microstructure Laboratory for maintaining the cleanroom, which is crucial and fundamental for the research in this thesis. They include Dr. Stefan Nygren, Dr. Örjan Vallin, Sven Norén, Dr. Amit Patel, Dr. Milena de Albuquerque Moreira, Dr. Björn Kuzavas, and Dr. Fredric Ericson.

The papers included in this thesis would not have been possible without the contributions of external collaborators. I am grateful for the efforts of Assoc. Prof. Carl Hägglund, Assoc. Prof. Ilya Sychugov, Xi Lu, Dr. André Görgens, Prof. Hyun Jae Kim, Jong Bin An, and Sujin Lee.

Special thanks to Prof. Zhen Zhang and Dr. Roger Karlsson for reviewing my thesis and providing helpful suggestions for its improvement.

Thanks to the financial support for this project from the Swedish Research Council (Vetenskapsrådet, 2018-03494) and Myfab Uppsala for providing facilities and experimental support.

Beside my research life, I want to thank my friends for their companionship and the happy moments we've shared. They include Assoc. Prof. Lichuan Wu, Dr. Hongling Yu, Kanglei Pang, Ruoqi Zhang, Dr. Hanqing Zhang, and all the friends with whom I play badminton.

Last but foremost, I want to express my deepest love and gratitude to my wife, Die Wang. Your love, care, support, tolerance, and companionship have been my anchor throughout this journey, enabling me to pursue my dream in Sweden and go through the darkness. Thanks to my parents' love, support, and understandings in my growth.

Thank you all!

8 References:

[1] C. E. Hall, “Method for the Observation of Macromolecules with the Electron Microscope Illustrated with Micrographs of DNA,” *J Cell Biol*, vol. 2, no. 5, pp. 625–628, Sep. 1956, doi: 10.1083/jcb.2.5.625.

[2] N. Akkilic, S. Geschwindner, and F. Höök, “Single-molecule biosensors: Recent advances and applications,” *Biosens Bioelectron*, vol. 151, pp. 111944, Mar. 2020, doi: 10.1016/j.bios.2019.111944.

[3] Z. Su, T. Li, D. Wu, Y. Wu, and G. Li, “Recent Progress on Single-Molecule Detection Technologies for Food Safety,” *J Agric Food Chem*, vol. 70, no. 2, pp. 458–469, Jan. 2022, doi: 10.1021/acs.jafc.1c06808.

[4] Y. Ishii and T. Yanagida, “Single Molecule Detection in Life Sciences,” *Single Molecules*, vol. 1, no. 1, pp. 5–16, Apr. 2000, doi: 10.1002/(SICI)1438-5171(200004)1:1<5::AID-SIMO5>3.0.CO;2-A.

[5] Zander C, Enderlein J, and Keller R A., *Single molecule detection in solution: methods and applications*. Wiley, 2002.

[6] W. E. Moerner, Y. Shechtman, and Q. Wang, “Single-molecule spectroscopy and imaging over the decades,” *Faraday Discuss*, vol. 184, pp. 9–36, 2015, doi: 10.1039/C5FD00149H.

[7] M. Orrit and J. Bernard, “Single pentacene molecules detected by fluorescence excitation in a *p* -terphenyl crystal,” *Phys Rev Lett*, vol. 65, no. 21, pp. 2716–2719, Nov. 1990, doi: 10.1103/PhysRevLett.65.2716.

[8] J. R. Lakowicz, “Principles of Fluorescence Spectroscopy Third Edition.” Springer, New York, NY, USA, 2006.

[9] M. J. Sanderson, I. Smith, I. Parker, and M. D. Bootman, “Fluorescence Microscopy,” *Cold Spring Harb Protoc*, vol. 2014, no. 10, pp. 1042–1064, Oct. 2014, doi: 10.1101/pdb.top071795.

[10] W. E. Moerner and D. P. Fromm, “Methods of single-molecule fluorescence spectroscopy and microscopy,” *Review of Scientific Instruments*, vol. 74, no. 8, pp. 3597–3619, Aug. 2003, doi: 10.1063/1.1589587.

[11] Th. Basché, W. P. Ambrose, and W. E. Moerner, “Optical spectra and kinetics of single impurity molecules in a polymer: spectral diffusion and persistent spectral hole burning,” *Journal of the Optical Society of America B*, vol. 9, no. 5, p. 829, May 1992, doi: 10.1364/JOSAB.9.000829.

[12] S. Shashkova and M. C. Leake, “Single-molecule fluorescence microscopy review: shedding new light on old problems,” *Biosci Rep*, vol. 37, no. 4, Aug. 2017, doi: 10.1042/BSR20170031.

[13] S. Weiss, “Fluorescence Spectroscopy of Single Biomolecules,” *Science (1979)*, vol. 283, no. 5408, pp. 1676–1683, Mar. 1999, doi: 10.1126/science.283.5408.1676.

[14] T. Ha, T. Enderle, D. F. Ogletree, D. S. Chemla, P. R. Selvin, and S. Weiss, “Probing the interaction between two single molecules: fluorescence resonance energy transfer between a single donor and a single acceptor.,” *Proceedings of the National Academy of Sciences*, vol. 93, no. 13, pp. 6264–6268, Jun. 1996, doi: 10.1073/pnas.93.13.6264.

[15] C. Li, Y. Li, Y. Zhang, and C. Zhang, “Single-molecule fluorescence resonance energy transfer and its biomedical applications,” *TrAC Trends in Analytical Chemistry*, vol. 122, p. 115753, Jan. 2020, doi: 10.1016/j.trac.2019.115753.

[16] E. Lerner *et al.*, “Toward dynamic structural biology: Two decades of single-molecule Förster resonance energy transfer,” *Science (1979)*, vol. 359, no. 6373, Jan. 2018, doi: 10.1126/science.aan1133.

[17] Edinburgh Instruments, “Two-photon fluorescence microscopy with the RMS1000 confocal microscope,” https://www.edinst.com/two-photon-fluorescence-microscopy-with-the-rms1000-confocal-microscope/

[18] W. Cao *et al.*, “The future transistors,” *Nature*, vol. 620, no. 7974, pp. 501–515, Aug. 2023, doi: 10.1038/s41586-023-06145-x.

[19] Y. Cui, Q. Wei, H. Park, and C. M. Lieber, “Nanowire Nanosensors for Highly Sensitive and Selective Detection of Biological and Chemical Species,” *Science (1979)*, vol. 293, no. 5533, pp. 1289–1292, Aug. 2001, doi: 10.1126/science.1062711.

[20] S. Sorgenfrei *et al.*, “Label-free single-molecule detection of DNA-hybridization kinetics with a carbon nanotube field-effect transistor,” *Nat Nanotechnol*, vol. 6, no. 2, pp. 126–132, Feb. 2011, doi: 10.1038/nnano.2010.275.

[21] F. Patolsky, G. Zheng, O. Hayden, M. Lakadamyali, X. Zhuang, and C. M. Lieber, “Electrical detection of single viruses,” *Proceedings of the National Academy of Sciences*, vol. 101, no. 39, pp. 14017–14022, Sep. 2004, doi: 10.1073/pnas.0406159101.

[22] F. Patolsky, G. Zheng, and C. M. Lieber, “Nanowire Sensors for Medicine and The Life Sciences,” *Nanomedicine*, vol. 1, no. 1, pp. 51–65, Jun. 2006, doi: 10.2217/17435889.1.1.51.

[23] A. Zhang, G. Zheng, and C. M. Lieber, “NanoScience and Technology Nanowires Building Blocks for Nanoscience and Nanotechnology.” [Online]. Available: http://www.springer.com/series/3705

[24] E. Stern, R. Wagner, F. J. Sigworth, R. Breaker, T. M. Fahmy, and M. A. Reed, “Importance of the Debye Screening Length on Nanowire Field Effect Transistor Sensors,” *Nano Lett*, vol. 7, no. 11, pp. 3405–3409, Nov. 2007, doi: 10.1021/nl071792z.

[25] K. Nomura, H. Ohta, A. Takagi, T. Kamiya, M. Hirano, and H. Hosono, “Room-temperature fabrication of transparent flexible thin-film transistors using amorphous oxide semiconductors,” *Nature*, vol. 432, no. 7016, pp. 488–492, Nov. 2004, doi: 10.1038/nature03090.

[26] Y. Zhu, Y. He, S. Jiang, L. Zhu, C. Chen, and Q. Wan, “Indium–gallium–zinc–oxide thin-film transistors: Materials, devices, and applications,” *Journal of Semiconductors*, vol. 42, no. 3, p. 031101, Mar. 2021, doi: 10.1088/1674-4926/42/3/031101.

[27] H. Yoo, I. S. Lee, S. Jung, S. M. Rho, B. H. Kang, and H. J. Kim, “A Review of Phototransistors Using Metal Oxide Semiconductors: Research Progress and Future Directions,” *Advanced Materials*, vol. 33, no. 47, Nov. 2021, doi: 10.1002/adma.202006091.

[28] B. H. Kang, W.-G. Kim, J. Chung, J. H. Lee, and H. J. Kim, “Simple Hydrogen Plasma Doping Process of Amorphous Indium Gallium Zinc Oxide-Based Phototransistors for Visible Light Detection,” *ACS Appl Mater Interfaces*, vol. 10, no. 8, pp. 7223–7230, Feb. 2018, doi: 10.1021/acsami.7b17897.

[29] M. Haase and H. Schäfer, “Upconverting Nanoparticles,” *Angewandte Chemie International Edition*, vol. 50, no. 26, pp. 5808–5829, Jun. 2011, doi: 10.1002/anie.201005159.

[30] W. Zheng, P. Huang, D. Tu, E. Ma, H. Zhu, and X. Chen, “Lanthanide-doped upconversion nano-bioprobes: electronic structures, optical properties, and biodetection,” *Chem Soc Rev*, vol. 44, no. 6, pp. 1379–1415, 2015, doi: 10.1039/C4CS00178H.

[31] M. Lin *et al.*, “Recent advances in synthesis and surface modification of lanthanide-doped upconversion nanoparticles for biomedical applications,” *Biotechnol Adv*, vol. 30, no. 6, pp. 1551–1561, Nov. 2012, doi: 10.1016/j.biotechadv.2012.04.009.

[32] F. Wang, J. Wang, and X. Liu, “Direct Evidence of a Surface Quenching Effect on Size-Dependent Luminescence of Upconversion Nanoparticles,” *Angewandte Chemie International Edition*, vol. 49, no. 41, pp. 7456–7460, Oct. 2010, doi: 10.1002/anie.201003959.

[33] S. Heer, K. Kömpe, H. -U. Güdel, and M. Haase, “Highly Efficient Multicolour Upconversion Emission in Transparent Colloids of Lanthanide-Doped $NaYF_4$ Nanocrystals,” *Advanced Materials*, vol. 16, no. 23–24, pp. 2102–2105, Dec. 2004, doi: 10.1002/adma.200400772.

[34] Q. Liu, Y. Zhang, C. S. Peng, T. Yang, L.-M. Joubert, and S. Chu, “Single upconversion nanoparticle imaging at sub-10 W cm−2 irradiance,” *Nat Photonics*, vol. 12, no. 9, pp. 548–553, Sep. 2018, doi: 10.1038/s41566-018-0217-1.

[35] I. L. Medintz and Niko. Hildebrandt, *FRET - Förster resonance energy transfer: from theory to applications*. Wiley-VCH Verlag GmbH, 2014.

[36] G. Chen, F. Song, X. Xiong, and X. Peng, “Fluorescent Nanosensors Based on Fluorescence Resonance Energy Transfer (FRET),” *Ind Eng Chem Res*, vol. 52, no. 33, pp. 11228–11245, Aug. 2013, doi: 10.1021/ie303485n.

[37] H. C. Ishikawa-Ankerhold, R. Ankerhold, and G. P. C. Drummen, “Advanced Fluorescence Microscopy Techniques—FRAP, FLIP, FLAP, FRET and FLIM,” *Molecules*, vol. 17, no. 4, pp. 4047–4132, Apr. 2012, doi: 10.3390/molecules17044047.

[38] A. V Zayats and I. I. Smolyaninov, “Near-field photonics: surface plasmon polaritons and localized surface plasmons,” *Journal of Optics A: Pure and Applied Optics*, vol. 5, no. 4, pp. S16–S50, Jul. 2003, doi: 10.1088/1464-4258/5/4/353.

[39] J. Zhang and L. Zhang, “Nanostructures for surface plasmons,” *Adv Opt Photonics*, vol. 4, no. 2, p. 157, Jun. 2012, doi: 10.1364/AOP.4.000157.

[40] M. Bauch, K. Toma, M. Toma, Q. Zhang, and J. Dostalek, “Plasmon-Enhanced Fluorescence Biosensors: a Review,” *Plasmonics*, vol. 9, no. 4, pp. 781–799, Aug. 2014, doi: 10.1007/s11468-013-9660-5.

[41] T. Ming, H. Chen, R. Jiang, Q. Li, and J. Wang, “Plasmon-Controlled Fluorescence: Beyond the Intensity Enhancement,” *J Phys Chem Lett*, vol. 3, no. 2, pp. 191–202, Jan. 2012, doi: 10.1021/jz201392k.

[42] W. Deng and E. M. Goldys, “Plasmonic Approach to Enhanced Fluorescence for Applications in Biotechnology and the Life Sciences,” *Langmuir*, vol. 28, no. 27, pp. 10152–10163, Jul. 2012, doi: 10.1021/la300332x.

[43] D. M. Wu, A. García-Etxarri, A. Salleo, and J. A. Dionne, “Plasmon-Enhanced Upconversion,” *J Phys Chem Lett*, vol. 5, no. 22, pp. 4020–4031, Nov. 2014, doi: 10.1021/jz5019042.

[44] Y. Meng *et al.*, “Bright single-nanocrystal upconversion at sub 0.5 W cm−2 irradiance via coupling to single nanocavity mode,” *Nat Photonics*, vol. 17, no. 1, pp. 73–81, Jan. 2023, doi: 10.1038/s41566-022-01101-z.

[45] S.-Y. Huang *et al.*, “Improvement in the bias stability of amorphous InGaZnO TFTs using an Al 2 O 3 passivation layer,” *Surf Coat Technol*, vol. 231, pp. 117–121, Sep. 2013, doi: 10.1016/j.surfcoat.2011.12.047.

[46] D. C. Corsino, J. P. S. Bermundo, M. N. Fujii, K. Takahashi, Y. Ishikawa, and Y. Uraoka, “Dimethylaluminum hydride for atomic layer deposition of Al $_2$ O $_3$ passivation for amorphous InGaZnO thin-film transistors,” *Applied Physics Express*, vol. 11, no. 6, p. 061103, Jun. 2018, doi: 10.7567/APEX.11.061103.

[47] Sze S. M.; Li Y.; Ng K. K. Physics of semiconductor devices, John wiley & sons, 2021.

[48] L. A. Ruiz-Taylor, T. L. Martin, and P. Wagner, “X-ray Photoelectron Spectroscopy and Radiometry Studies of Biotin-Derivatized Poly(l-lysine)-grafted-Poly(ethylene glycol) Monolayers on Metal Oxides,” *Langmuir*, vol. 17, no. 23, pp. 7313–7322, Nov. 2001, doi: 10.1021/la010620t.

[49] Y. Cui and C. M. Lieber, “Functional Nanoscale Electronic Devices Assembled Using Silicon Nanowire Building Blocks,” *Science (1979)*, vol. 291, no. 5505, pp. 851–853, Feb. 2001, doi: 10.1126/science.291.5505.851.

[50] Y. Zheng, G. Li, W. Wang, X. Li, and Z. Jiang, “Dry Etching Characteristics of Amorphous Indium-Gallium-Zinc-Oxide Thin Films,” *Plasma Science and Technology*, vol. 14, no. 10, pp. 915–918, Oct. 2012, doi: 10.1088/1009-0630/14/10/11.

[51] M. J. Levene, J. Korlach, S. W. Turner, M. Foquet, H. G. Craighead, and W. W. Webb, “Zero-Mode Waveguides for Single-Molecule Analysis at High Concentrations,” *Science (1979)*, vol. 299, no. 5607, pp. 682–686, Jan. 2003, doi: 10.1126/science.1079700.

[52] G. M. Crouch, D. Han, and P. W. Bohn, “Zero-mode waveguide nanophotonic structures for single molecule characterization,” *J Phys D Appl Phys*, vol. 51, no. 19, p. 193001, May 2018, doi: 10.1088/1361-6463/aab8be.

[53] H. Rigneault *et al.*, “Enhancement of Single-Molecule Fluorescence Detection in Subwavelength Apertures,” *Phys Rev Lett*, vol. 95, no. 11, p. 117401, Sep. 2005, doi: 10.1103/PhysRevLett.95.117401.

[54] P. Ghenuche, J. de Torres, S. B. Moparthi, V. Grigoriev, and J. Wenger, “Nanophotonic Enhancement of the Förster Resonance Energy-Transfer Rate with Single Nanoapertures,” *Nano Lett*, vol. 14, no. 8, pp. 4707–4714, Aug. 2014, doi: 10.1021/nl5018145.

[55] J. Eid *et al.*, “Real-Time DNA Sequencing from Single Polymerase Molecules,” *Science (1979)*, vol. 323, no. 5910, pp. 133–138, Jan. 2009, doi: 10.1126/science.1162986.
[56] M. Wu *et al.*, “Fluorescence enhancement in an over-etched gold zero-mode waveguide,” *Opt Express*, vol. 27, no. 13, p. 19002, Jun. 2019, doi: 10.1364/OE.27.019002.
[57] D. Punj *et al.*, “A plasmonic ‘antenna-in-box’ platform for enhanced single-molecule analysis at micromolar concentrations,” *Nat Nanotechnol*, vol. 8, no. 7, pp. 512–516, Jul. 2013, doi: 10.1038/nnano.2013.98.
[58] C. B. Murray, D. J. Norris, and M. G. Bawendi, “Synthesis and characterization of nearly monodisperse CdE (E = sulfur, selenium, tellurium) semiconductor nanocrystallites,” *J Am Chem Soc*, vol. 115, no. 19, pp. 8706–8715, Sep. 1993, doi: 10.1021/ja00072a025.
[59] F. P. García de Arquer, D. V. Talapin, V. I. Klimov, Y. Arakawa, M. Bayer, and E. H. Sargent, “Semiconductor quantum dots: Technological progress and future challenges,” *Science (1979)*, vol. 373, no. 6555, Aug. 2021, doi: 10.1126/science.aaz8541.
[60] N. Hildebrandt *et al.*, “Energy Transfer with Semiconductor Quantum Dot Bioconjugates: A Versatile Platform for Biosensing, Energy Harvesting, and Other Developing Applications,” *Chem Rev*, vol. 117, no. 2, pp. 536–711, Jan. 2017, doi: 10.1021/acs.chemrev.6b00030.
[61] C.-Y. Zhang, H.-C. Yeh, M. T. Kuroki, and T.-H. Wang, “Single-quantum-dot-based DNA nanosensor,” *Nat Mater*, vol. 4, no. 11, pp. 826–831, Nov. 2005, doi: 10.1038/nmat1508.
[62] O. Kulakovich *et al.*, “Enhanced Luminescence of CdSe Quantum Dots on Gold Colloids,” *Nano Lett*, vol. 2, no. 12, pp. 1449–1452, Dec. 2002, doi: 10.1021/nl025819k.
[63] W. Zhang, M. Caldarola, X. Lu, and M. Orrit, “Plasmonic Enhancement of Two-Photon-Excited Luminescence of Single Quantum Dots by Individual Gold Nanorods,” *ACS Photonics*, vol. 5, no. 7, pp. 2960–2968, Jul. 2018, doi: 10.1021/acsphotonics.8b00306.
[64] A. G. Brolo *et al.*, “Surface Plasmon−Quantum Dot Coupling from Arrays of Nanoholes,” *J Phys Chem B*, vol. 110, no. 16, pp. 8307–8313, Apr. 2006, doi: 10.1021/jp054129c.
[65] A. Al Masud *et al.*, “Photoluminescence Enhancement, Blinking Suppression, and Improved Biexciton Quantum Yield of Single Quantum Dots in Zero Mode Waveguides,” *J Phys Chem Lett*, vol. 12, no. 13, pp. 3303–3311, Apr. 2021, doi: 10.1021/acs.jpclett.1c00450.
[66] Q. Jiang, P. Roy, J.-B. Claude, and J. Wenger, “Single Photon Source from a Nanoantenna-Trapped Single Quantum Dot,” *Nano Lett*, vol. 21, no. 16, pp. 7030–7036, Aug. 2021, doi: 10.1021/acs.nanolett.1c02449.
[67] A. G. Curto, G. Volpe, T. H. Taminiau, M. P. Kreuzer, R. Quidant, and N. F. van Hulst, “Unidirectional Emission of a Quantum Dot Coupled to a Nanoantenna,” *Science (1979)*, vol. 329, no. 5994, pp. 930–933, Aug. 2010, doi: 10.1126/science.1191922.
[68] M. Schwind, B. Kasemo, and I. Zorić, “Localized and Propagating Plasmons in Metal Films with Nanoholes,” *Nano Lett*, vol. 13, no. 4, pp. 1743–1750, Apr. 2013, doi: 10.1021/nl400328x.
[69] L. Wu, P. Bai, X. Zhou, and E. P. Li, “Reflection and Transmission Modes in Nanohole-Array-Based Plasmonic Sensors,” *IEEE*

Photonics J, vol. 4, no. 1, pp. 26–33, Feb. 2012, doi: 10.1109/JPHOT.2011.2177652.

[70] J. Korlach *et al.*, "Selective aluminum passivation for targeted immobilization of single DNA polymerase molecules in zero-mode waveguide nanostructures," *Proceedings of the National Academy of Sciences*, vol. 105, no. 4, pp. 1176–1181, Jan. 2008, doi: 10.1073/pnas.0710982105.

[71] P. Vader, X. O. Breakefield, and M. J. A. Wood, "Extracellular vesicles: emerging targets for cancer therapy," *Trends Mol Med*, vol. 20, no. 7, pp. 385–393, Jul. 2014, doi: 10.1016/j.molmed.2014.03.002.

[72] S. Cavallaro *et al.*, "Multiparametric Profiling of Single Nanoscale Extracellular Vesicles by Combined Atomic Force and Fluorescence Microscopy: Correlation and Heterogeneity in Their Molecular and Biophysical Features," *Small*, vol. 17, no. 14, Apr. 2021, doi: 10.1002/smll.202008155.

[73] D. Huang *et al.*, "Advances in Biological Function and Clinical Application of Small Extracellular Vesicle Membrane Proteins," *Front Oncol*, vol. 11, May 2021, doi: 10.3389/fonc.2021.675940.

[74] M. Jørgensen, R. Bæk, S. Pedersen, E. K. L. Søndergaard, S. R. Kristensen, and K. Varming, "Extracellular Vesicle (EV) Array: microarray capturing of exosomes and other extracellular vesicles for multiplexed phenotyping," *J Extracell Vesicles*, vol. 2, no. 1, Jan. 2013, doi: 10.3402/jev.v2i0.20920.

[75] A. Prasad, J. Choi, Z. Jia, S. Park, and M. R. Gartia, "Nanohole array plasmonic biosensors: Emerging point-of-care applications," *Biosens Bioelectron*, vol. 130, pp. 185–203, Apr. 2019, doi: 10.1016/j.bios.2019.01.037.

[76] J. Min *et al.*, "Plasmon-Enhanced Biosensing for Multiplexed Profiling of Extracellular Vesicles," *Adv Biosyst*, vol. 4, no. 12, Dec. 2020, doi: 10.1002/adbi.202000003.

[77] E. Le Moal, E. Fort, S. Lévêque-Fort, F. P. Cordelières, M.-P. Fontaine-Aupart, and C. Ricolleau, "Enhanced Fluorescence Cell Imaging with Metal-Coated Slides," *Biophys J*, vol. 92, no. 6, pp. 2150–2161, Mar. 2007, doi: 10.1529/biophysj.106.096750.

[78] J. Zhao *et al.*, "Single-nanocrystal sensitivity achieved by enhanced upconversion luminescence," *Nat Nanotechnol*, vol. 8, no. 10, pp. 729–734, Oct. 2013, doi: 10.1038/nnano.2013.171.

[79] D. J. Gargas *et al.*, "Engineering bright sub-10-nm upconverting nanocrystals for single-molecule imaging," *Nat Nanotechnol*, vol. 9, no. 4, pp. 300–305, Apr. 2014, doi: 10.1038/nnano.2014.29.

[80] S. Schietinger, T. Aichele, H.-Q. Wang, T. Nann, and O. Benson, "Plasmon-Enhanced Upconversion in Single $NaYF_4$:Yb^{3+}/Er^{3+} Co-doped Nanocrystals," *Nano Lett*, vol. 10, no. 1, pp. 134–138, Jan. 2010, doi: 10.1021/nl903046r.

[81] Y. Xue *et al.*, "Tuning Plasmonic Enhancement of Single Nanocrystal Upconversion Luminescence by Varying Gold Nanorod Diameter," *Small*, vol. 13, no. 36, Sep. 2017, doi: 10.1002/smll.201701155.

[82] Y. Gao, S. Murai, F. Zhang, S. Tamura, K. Tomita, and K. Tanaka, "Enhancing upconversion photoluminescence by plasmonic-photonic hybrid mode," *Opt Express*, vol. 28, no. 2, p. 886, Jan. 2020, doi: 10.1364/OE.379314.

[83] M. Saboktakin, X. Ye, U. K. Chettiar, N. Engheta, C. B. Murray, and C. R. Kagan, “Plasmonic Enhancement of Nanophosphor Upconversion Luminescence in Au Nanohole Arrays,” *ACS Nano*, vol. 7, no. 8, pp. 7186–7192, Aug. 2013, doi: 10.1021/nn402598e.

[84] E. Verhagen, L. Kuipers, and A. Polman, “Field enhancement in metallic subwavelength aperture arrays probed by erbium upconversion luminescence,” *Opt Express*, vol. 17, no. 17, p. 14586, Aug. 2009, doi: 10.1364/OE.17.014586.

[85] D. Lu, S. K. Cho, S. Ahn, L. Brun, C. J. Summers, and W. Park, “Plasmon Enhancement Mechanism for the Upconversion Processes in $NaYF_4$:Yb^{3+},Er^{3+} Nanoparticles: Maxwell *versus* Förster,” *ACS Nano*, vol. 8, no. 8, pp. 7780–7792, Aug. 2014, doi: 10.1021/nn5011254.

[86] Y. Wu *et al.*, “Upconversion superburst with sub-2 μs lifetime,” *Nat Nanotechnol*, vol. 14, no. 12, pp. 1110–1115, Dec. 2019, doi: 10.1038/s41565-019-0560-5.

[87] C. Mao *et al.*, “Enhanced Upconversion Luminescence by Two-Dimensional Photonic Crystal Structure,” *ACS Photonics*, vol. 6, no. 8, pp. 1882–1888, Aug. 2019, doi: 10.1021/acsphotonics.9b00756.

[88] N. J. Greybush *et al.*, “Plasmon-Enhanced Upconversion Luminescence in Single Nanophosphor–Nanorod Heterodimers Formed through Template-Assisted Self-Assembly,” *ACS Nano*, vol. 8, no. 9, pp. 9482–9491, Sep. 2014, doi: 10.1021/nn503675a.

[89] R. Schlapak, J. Danzberger, T. Haselgrübler, P. Hinterdorfer, F. Schäffler, and S. Howorka, “Painting with Biomolecules at the Nanoscale: Biofunctionalization with Tunable Surface Densities,” *Nano Lett*, vol. 12, no. 4, pp. 1983–1989, Apr. 2012, doi: 10.1021/nl2045414.

[90] S. Li, S. Zeng, L. Chen, Z. Zhang, K. Hjort, and S.-L. Zhang, “Nanoarrays on Passivated Aluminum Surface for Site-Specific Immobilization of Biomolecules,” *ACS Appl Bio Mater*, vol. 1, no. 1, pp. 125–135, Jul. 2018, doi: 10.1021/acsabm.8b00037.

[91] K. Imura, T. Nagahara, and H. Okamoto, “Near-Field Two-Photon-Induced Photoluminescence from Single Gold Nanorods and Imaging of Plasmon Modes,” *J Phys Chem B*, vol. 109, no. 27, pp. 13214–13220, Jul. 2005, doi: 10.1021/jp051631o.

[92] D. V. Pominova *et al.*, “Upconversion microparticles as time-resolved luminescent probes for multiphoton microscopy: desired signal extraction from the streaking effect,” *J Biomed Opt*, vol. 21, no. 9, p. 096002, Sep. 2016, doi: 10.1117/1.JBO.21.9.096002.

Acta Universitatis Upsaliensis

Digital Comprehensive Summaries of Uppsala Dissertations from the Faculty of Science and Technology 2451

Editor: The Dean of the Faculty of Science and Technology

A doctoral dissertation from the Faculty of Science and Technology, Uppsala University, is usually a summary of a number of papers. A few copies of the complete dissertation are kept at major Swedish research libraries, while the summary alone is distributed internationally through the series Digital Comprehensive Summaries of Uppsala Dissertations from the Faculty of Science and Technology. (Prior to January, 2005, the series was published under the title "Comprehensive Summaries of Uppsala Dissertations from the Faculty of Science and Technology".)

Distribution: publications.uu.se
urn:nbn:se:uu:diva-538768

ACTA UNIVERSITATIS
UPSALIENSIS
2024